Effective Fetch and Duration of Tropical Cyclone Wind Fields Estimated from Simultaneous Wind and Wave Measurements: Surface Wave and Air–Sea Exchange Computation

PAUL A. HWANG

Remote Sensing Division, Naval Research Laboratory, Washington, D.C.

YALIN FAN

Oceanography Division, Naval Research Laboratory, Stennis Space Center, Mississippi

(Manuscript received 3 August 2016, in final form 10 November 2016)

ABSTRACT

Simultaneous wind and wave measurements have been obtained inside tropical cyclones in several hurricane hunter missions. Analyses of these datasets show that the surface wave development inside hurricanes follows essentially the same duration- and fetch-limited growth functions established in steady wind forcing conditions. This paper explores the application of several parameterization functions of wind-wave systems to quantify the energy and momentum exchanges inside hurricanes from an initially limited input of the environmental parameters, such as the wind field alone. A critical prerequisite to applying the wind-wave growth functions is the knowledge of fetch and duration for the hurricane wind field. Four sets of simultaneous wind and wave measurements from hurricane hunter missions are analyzed to derive a fetch and duration scaling model. Time series of 2D hurricane wind fields can then be used to investigate the detailed spatial distribution and temporal evolution of the sea state parameters and the associated air–sea energy and momentum exchanges following the hurricane development.

1. Introduction

Tropical cyclones are among the most powerful natural phenomena. They bring very strong winds over an area several hundred kilometers in diameter. In the ocean, the strong winds generate high waves. The wind and wave actions produce tremendous air–sea exchanges.

Many analyses of wind and wave measurements under hurricane conditions have shown that fetch- and duration-limited wave growth functions derived from steady wind forcing conditions are applicable to the wave fields generated by hurricanes (Young 1988, 1998, 2003, 2006; Young and Burchell 2006; Young and Vinoth 2013; Hwang 2016; Hwang and Walsh 2016). For the fetch- and duration-limited wave systems, the wind-wave triplets (reference wind speed U_{10}, significant wave height H_s, and spectral peak wave period T_p) are closely related. Given the fetch or duration information, the full set of the triplets can be computed knowing any one of the three because the fetch- or duration-limited wave growth functions supply two equations connecting the wind-wave triplets. In addition, the air–sea energy and momentum exchange rates through the wave motion, E_t and M_t, respectively, are functions of the wind-wave triplets. The ability to define the fetch and duration of the hurricane wind field thus provides a means to estimate the air–sea exchanges inside hurricanes based on an initially very limited input such as the wind field alone (Hwang 2016; Hwang and Walsh 2016).

In a case study of Hurricane Bonnie 1998 during its category 2 stage, the wind and wave measurements inside the hurricane are used to retrieve the effective fetch x_f and duration t_d (Hwang 2016; Hwang and Walsh 2016). The results show that x_f and t_d vary approximately linearly with the distance r to the measurement location from the hurricane center; the slope and intercept of the linear regression function vary systematically with the azimuth angle ϕ relative to the hurricane heading.

U.S. Naval Research Laboratory Publication Number JA/7260—16-0146.

Corresponding author e-mail: Dr. Paul A. Hwang, paul.hwang@nrl.navy.mil

DOI: 10.1175/JPO-D-16-0180.1

TABLE 1. Some basic information of the four datasets, collected in hurricane Bonnie 1998 (B24) and Ivan 2004 (I09, I12, and I14), used for the analysis in this paper; the headers U10, rm, ϕh, Hs, and Tp represent U_{10}, r_m, ϕ_h, H_s, and T_p.

Data ID	B24	I09	I12	I14
Start time	2029 UTC 24 Aug 1998	1615 UTC 9 Sep 2004	1039 UTC 12 Sep 2004	2009 UTC 14 Sep 2004
End time	0144 UTC 25 Aug 1998	2010 UTC 9 Sep 2004	1541 UTC 12 Sep 2004	0249 UTC 15 Sep 2004
HRD U10 max ($m\,s^{-1}$)	44.4	59.4	55.4	61.6
HRD rm (km)	74.0	13.0	17.0	42.0
Vh ($m\,s^{-1}$)	4.5	5.6	4.3	4.8
ϕh (°N)	13.0	62.0	66.0	25.0
SRA U10 min ($m\,s^{-1}$)	1.4	1.8	0.8	1.2
SRA U10 max ($m\,s^{-1}$)	45.7	74.0	59.9	69.6
SRA Hs min (m)	4.4	1.6	2.9	3.6
SRA Hs max (m)	10.9	12.7	12.0	13.1
SRA Tp min (s)	8.0	5.8	8.2	8.9
SRA Tp max (s)	13.3	15.2	13.8	14.4
# SRA spectra	233	376	456	600

In this paper, wind and wave measurements in four hurricane scenes are assembled for the purpose of constructing a fetch and duration scaling model applicable to a wider range of hurricanes. Section 2 describes the datasets. Section 3 presents the analysis and formulation of the fetch and duration scaling model. Section 4 illustrates an application of the fetch and duration scaling model to a time series of 2D hurricane wind fields to study the temporal evolution and spatial distribution of the energy and momentum exchanges following the hurricane progression. Also discussed in this section is the azimuthal and radial distributions of the wind and wave properties from hurricane hunter observations, and a comparison study of our fetch model with other published works. Section 5 is a summary.

2. Description of datasets

The four wind and wave datasets used for the present analysis are from the National Aeronautics and Space Administration (NASA) and National Oceanic and Atmospheric Administration (NOAA) combined hurricane hunter missions during Bonnie 1998 (Wright et al. 2001; Moon et al. 2003) and Ivan 2004 (Fan et al. 2009).

The NASA scanning radar altimeter (SRA) acquires 3D ocean surface topography. For hurricane hunter missions, the SRA typically produces the 3D topography at about 25-m horizontal resolution with a cross-track swath of about 1200-m coverage (Walsh et al. 1985, 1989; Wright et al. 2001). The surface topography is then used for computing the 2D wavenumber spectra of surface waves using the resampled 256 × 256 grids of 7-m spacing. The spectra are typically saved with an ensemble average of five consecutive segments, which is equivalent to about 9 km along the groundtrack for each spectrum.

The NOAA Hurricane Research Division (HRD) routinely produces observation-based surface wind analyses for hurricanes (e.g., Powell et al. 1996). The storm-centered analysis of the wind fields performed at HRD is incorporated with the wave data in real time (Wright et al. 2001).

Table 1 lists some basic information of the four datasets, including the start/stop time, hurricane advancing speed V_h and advancing direction ϕ_h estimated from the time series of the hurricane eye position, and the range (maximum and minimum) and number of the (U_{10}, H_s, and T_p) triplets in each dataset. The time series of hurricane wind fields will be further discussed in section 4b.

The first three columns of Fig. 1 show the wind-wave triplets (U_{10}, H_s, and T_p) of the four datasets in the order of B24, I09, I12, and I14 from top to bottom. These wind-wave datasets are typically composed of 6 to 12 transects radiating from the hurricane center plus several segments connecting the consecutive transects. In the fourth column, a 2D wind field is shown for each corresponding dataset. These 2D wind fields are selected at approximately the middle of the SRA data acquisition durations (I09, I12, and I14) or closest to the data acquisition duration when the middle-time wind field is not available (B24). The coordinates for all the displays in this paper have been rotated such that the hurricane heading is toward the top of the page. The maximum wind speed U_{10m} and the radius of maximum wind speed r_m based on these 2D wind fields are also listed in Table 1. In the subsequent analysis of the fetch and duration scaling model (section 3), the r_m based on the 2D wind fields are used except for dataset B24, for which we use the number (74 km) documented in Table 1 of Moon et al. (2003).

Figure 2 shows the similarity relation of the wind-wave triplets in terms of the dimensionless wave variance as a function of dimensionless frequency: $\eta_{\#}(\omega_{\#})$, where $\eta_{\#} = \eta^2_{\rm rms} g^2 U_{10}^{-4}$, $\omega_{\#} = \omega_p U_{10} g^{-1}$, and g is the gravitational acceleration; the root-mean-square (rms)

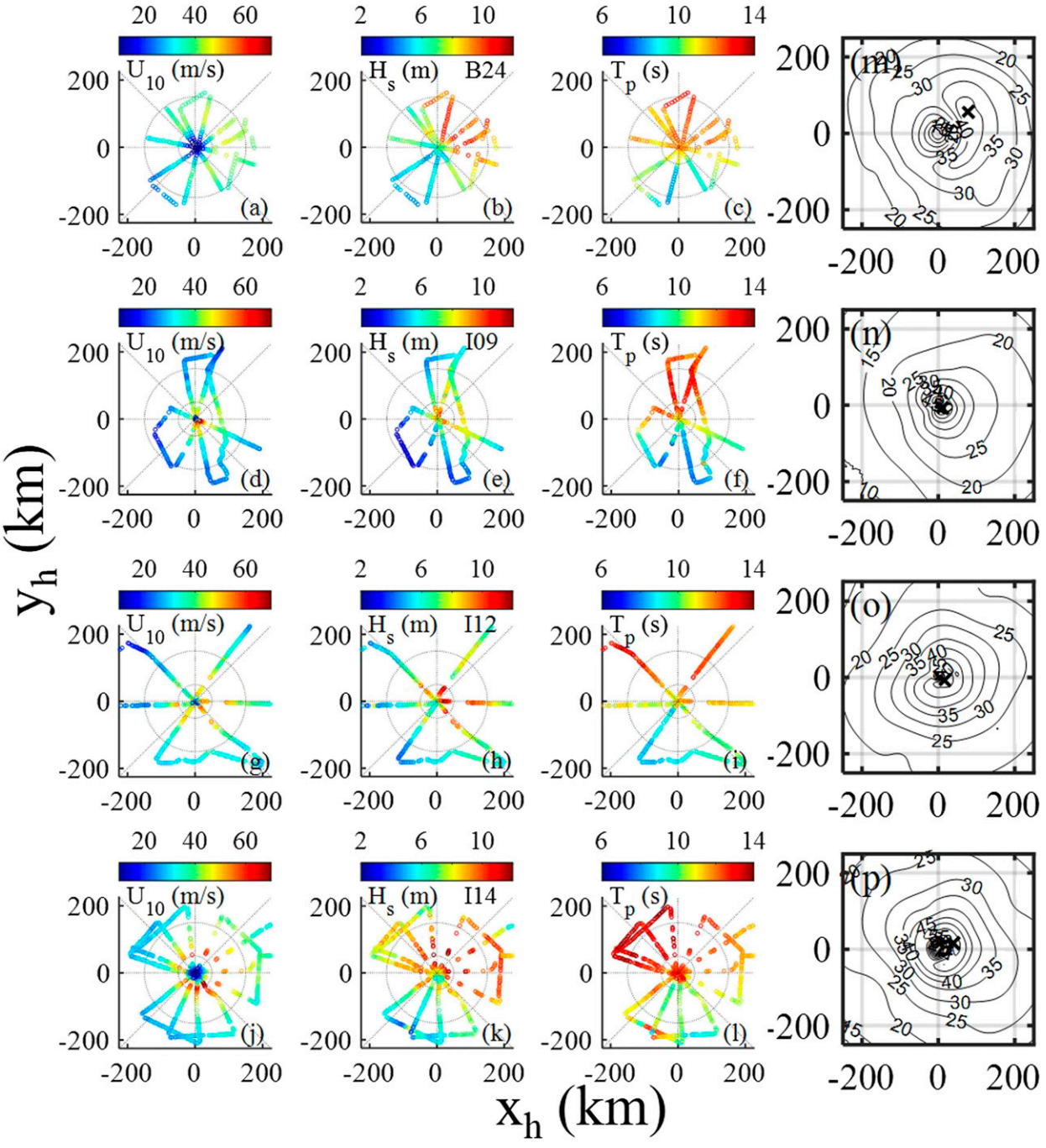

FIG. 1. Color-coded, wind-wave triplets inside hurricanes along several groundtracks: (column 1) U_{10}, (column 2) H_s, (column 3) T_p. (column 4) A representative 2D wind field for each case. (top to bottom) Cases B24, I09, I12, and I14 are arranged.

surface elevation $\eta_{\rm rms}$ is related to the significant wave height by $H_s = 4\eta_{\rm rms}$ and $\omega_p = 2\pi/T_p$. Superimposed in the background for reference are the results from a dataset (Burling 1959; Hasselmann et al. 1973; Donelan et al. 1985; Dobson et al. 1989; Babanin and Soloviev 1998; also known as BHDDB) combining five field experiments with quasi-steady winds and near-neutral stability conditions; the combined dataset covers a broad range of wave conditions, particularly the wave age (the inverse dimensionless frequency). The BHDDB dataset is used as the basis for establishing the first- and second-order fitted fetch- and duration-limited growth functions (Hwang and Wang 2004; Hwang 2006), which will be described further in section 3; the fitted growth

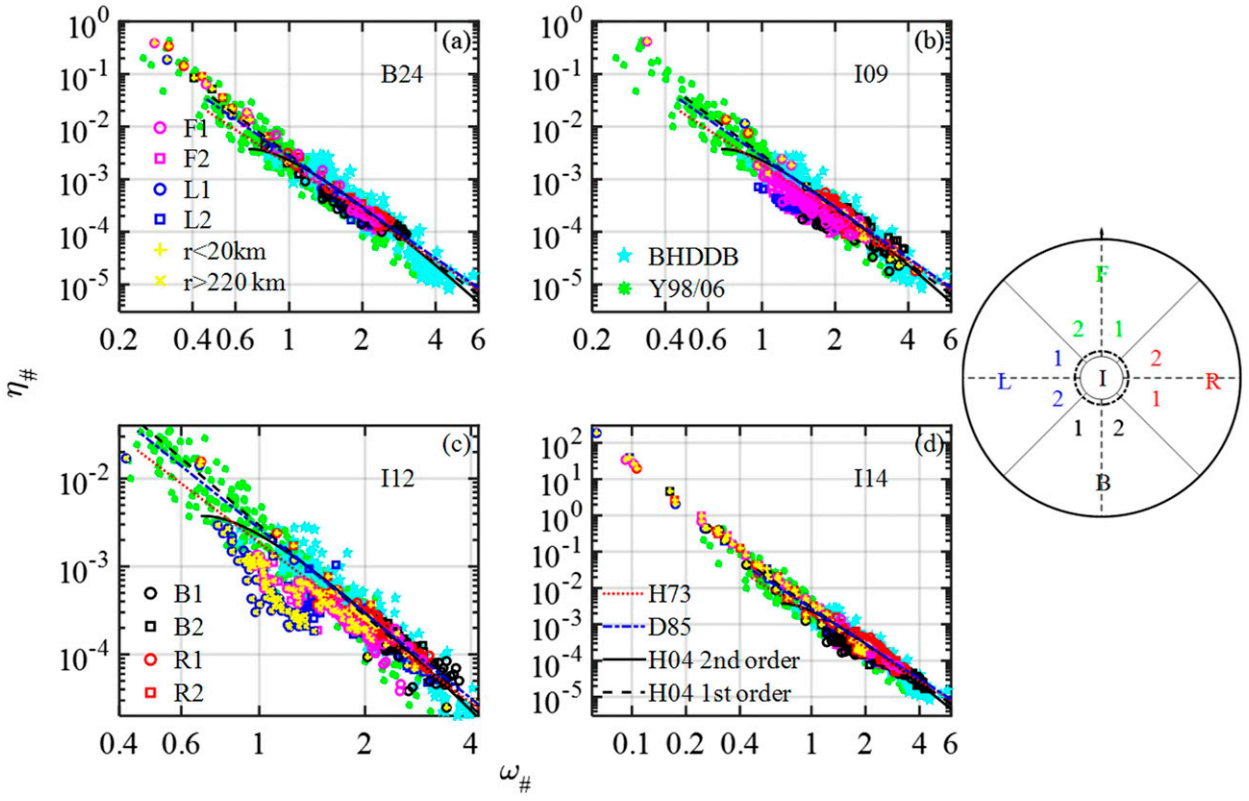

FIG. 2. The wave growth function in terms of $\eta_{\#}(\omega_{\#})$ for the surface waves inside hurricanes: (a) B24, (b) I09, (c) I12, and (d) I14. The data are shown with different symbols in eight pie-shaped slices: two slices in each of the four hurricane quarters [left (L); back (B); right (R); front (F)] shown in the inset. Measurements with $r < 20$ km and $r > 220$ km are marked with + and x, respectively. In the background are quasi-steady data BHDDB (light blue) and hurricane data from directional buoy recording (Y88/06: Young 1988, 2006; light green); the reference growth curves shown are dotted (H73: Hasselmann et al. 1973), dashed–dotted (D85: Donelan et al. 1985), and solid and dashed for the second- and first-order fittings through the BHDDB quasi-steady wind forcing data (H04: Hwang and Wang 2004).

functions are shown with dashed and solid curves in each panel.

Also plotted in the background with light green color are hurricane data collected by directional wave buoys in northwest coast of Australia over a period of more than 20 yr (Young 1998, 2006); the growth curves used in Young's (1988, 1998, 2006) discussions of hurricane waves are based on Hasselmann et al. (1973) and Donelan et al. (1985), which are also illustrated and labeled H73 and D85, respectively. Interestingly, the degrees of data scatter of the hurricane and steady wind datasets are not that different, and the growth curves derived from ideal (steady and homogeneous) wind-wave generation are applicable to both hurricane and steady wind data groups.

There are systematic differences in the agreement between the growth curves and the wind-wave measurements in different sectors of the hurricane coverage area. For convenience of comparison, the data are shown with eight different symbols (two for each quarter referenced to the hurricane heading; see inset). As observed in Hwang (2016, p. 47), based on analyzing a subset of B24 (60 spectra) reported in Wright et al. (2001), "The most variable wave conditions are in the backside of the hurricane, spanning the approximate upper and lower bounds of 'hyper' and 'hypo' growth conditions compared to the reference growth curves; with more hyper cases in the present measurements. In contrast, the wave conditions tend to be average to hyper in the right-hand sector and hypo in the left-hand sector." More extensive discussions are presented in the analysis of the full set of B24 data (Hwang and Walsh 2016). Similar conclusions on the fetch- and duration-limited nature of wave growth and azimuthal variation are applicable to the other three datasets. Data points showing large deviation from the growth curves are either very close or very far from the hurricane center, indicating severe swell contamination; these data points are marked with a + (for $r < 20$ km) and x (for $r > 220$ km). Further discussion of azimuthal and radial variation of the wind and wave properties inside hurricanes is given in section 4d.

3. Fetch and duration analysis

Fetch- or duration-limited wave growth functions constitute two dimensionless equations describing the development of characteristic wave height and wave period as a function of fetch or duration: $\eta_{\#}(x_{\#})$ and $\omega_{\#}(x_{\#})$ or $\eta_{\#}(t_{\#})$ and $\omega_{\#}(t_{\#})$. For gravity waves, the dimensionless parameters are given as $\eta_{\#} = \eta^2_{\rm rms} g^2 U_{10}^{-4} = H_s^2 g^2 (16 U_{10}^4)^{-1}$, $\omega_{\#} = 2\pi U_{10}(T_p g)^{-1}$, $x_{\#} = x_f g U_{10}^{-2}$, $t_{\#} = t_d g U_{10}^{-1}$, and $\eta^2_{\rm rms}$ is the variance of the ocean surface displacement. Keeping the wind-wave triplets (U_{10}, H_s, and T_p) explicitly in the equations, the fetch-limited condition can be expressed as (Hwang and Wang 2004; Hwang 2016)

$$\frac{H_s^2 g^2}{16 U_{10}^4} = 6.19 \times 10^{-7} \left(\frac{x_f g}{U_{10}^2}\right)^{0.81},$$
$$\frac{2\pi U_{10}}{T_p g} = 11.86 \left(\frac{x_f g}{U_{10}^2}\right)^{-0.24}. \quad (1)$$

Similarly, for the duration-limited condition,

$$\frac{H_s^2 g^2}{16 U_{10}^4} = 1.27 \times 10^{-8} \left(\frac{t_d g}{U_{10}}\right)^{1.06},$$
$$\frac{2\pi U_{10}}{T_p g} = 2.94 \left(\frac{t_d g}{U_{10}}\right)^{-0.34}. \quad (2)$$

The two similarity formulas allow the determination of the full set of the wind-wave triplets given only one of the three as input, subject to the condition that the fetch or duration is known for (1) or (2), respectively. Typically, these equations are used to obtain wave information (H_s and T_p) from wind input. Indeed, they have been used for wave forecast/hindcast prior to the advent of numerical wave models, and after numerical wave models become prevalent the fetch- and duration-limited wave growths are important benchmark tests for fine tuning the various source and sink functions.

The common fetch or duration parameters on the right-hand side of the pair of equations can be removed to produce a similarity relation of the wind-wave triplets sans fetch or duration:

$$\frac{H_s^2 g^2}{16 U_{10}^4} = 2.94 \times 10^{-3} \left(\frac{2\pi U_{10}}{T_p g}\right)^{-3.42}. \quad (3)$$

In the absence of fetch or duration measurements, (3) is a very useful diagnostic formula for discerning the wind–sea nature of a wave field.

As noted above, to use the wave growth functions (1) or (2), it is necessary to know the fetch or duration in addition to the wind input. For a water body with a well-defined land–water interface, the determination of the wind fetch is straightforward. Similarly, for a wind event that remains steady following a relatively sharp rise, the wind duration can be estimated reasonably accurately. It is, however, much more difficult to define the fetch or duration for the evolving hurricane wind field.

Making use of the wind-wave triplets measured inside Bonnier 1998 (Wright et al. 2001; Moon et al. 2003), Hwang (2016) and Hwang and Walsh (2016) retrieve the effective fetches and durations at the measurement locations inside the hurricane by rearranging the variables in (1) and (2):

$$x_{\eta x} = 4.24 \times 10^7 U_{10}^{-2.93} H_s^{2.47},$$
$$x_{\omega x} = 2.29 \times 10^4 U_{10}^{-2.22} T_p^{4.22}, \quad \text{and} \quad (4)$$
$$t_{\eta t} = 1.75 \times 10^4 U_{10}^{-2.77} H_s^{3.77},$$
$$t_{\omega t} = 4.81 \times 10^4 U_{10}^{-2.22} T_p^{3.22}. \quad (5)$$

As explained in Hwang and Walsh (2016), the wind generations in different quarters are not on equal footing because of the advancing wind field and differences in the base sea state from upstream feeding. To account for the observed systematic deviation from the reference growth curves of the hurricane wind waves in different sectors (Fig. 2), the fetches or durations for H_s and T_p are allowed to be different.

The results show that the effective fetch and duration increase about linearly with the distance r to the measurement location from the hurricane center. The slope s and intercept I of the linear function vary systematically with the azimuth angle ϕ referenced to the hurricane heading; all angles in this paper are positive counterclockwise (CCW):

$$x_{\eta x}(r,\phi) = s_{\eta x}(\phi) r + I_{\eta x}(\phi),$$
$$x_{\omega x}(r,\phi) = s_{\omega x}(\phi) r + I_{\omega x}(\phi), \quad \text{and} \quad (6)$$
$$t_{\eta t}(r,\phi) = s_{\eta t}(\phi) r + I_{\eta t}(\phi),$$
$$t_{\omega t}(r,\phi) = s_{\omega t}(\phi) r + I_{\omega t}(\phi). \quad (7)$$

Following the same procedure and applying the fetch and duration retrieval along flight transects (Fig. 1) of the four datasets listed in Table 1, the slopes and intercepts are shown in Fig. 3 with black squares; they are also listed in Table 2 (the headers s_ex, I_ex, s_ox, I_ox, s_et, I_et, s_ot, and I_ot represent $s_{\eta x}$, $I_{\eta x}$, $s_{\omega x}$, $I_{\omega x}$, $s_{\eta t}$, $I_{\eta t}$, $s_{\omega t}$ and $I_{\omega t}$). In the present analysis, we use the data with r between 50 and 160 km for linear fitting to minimize swell contamination

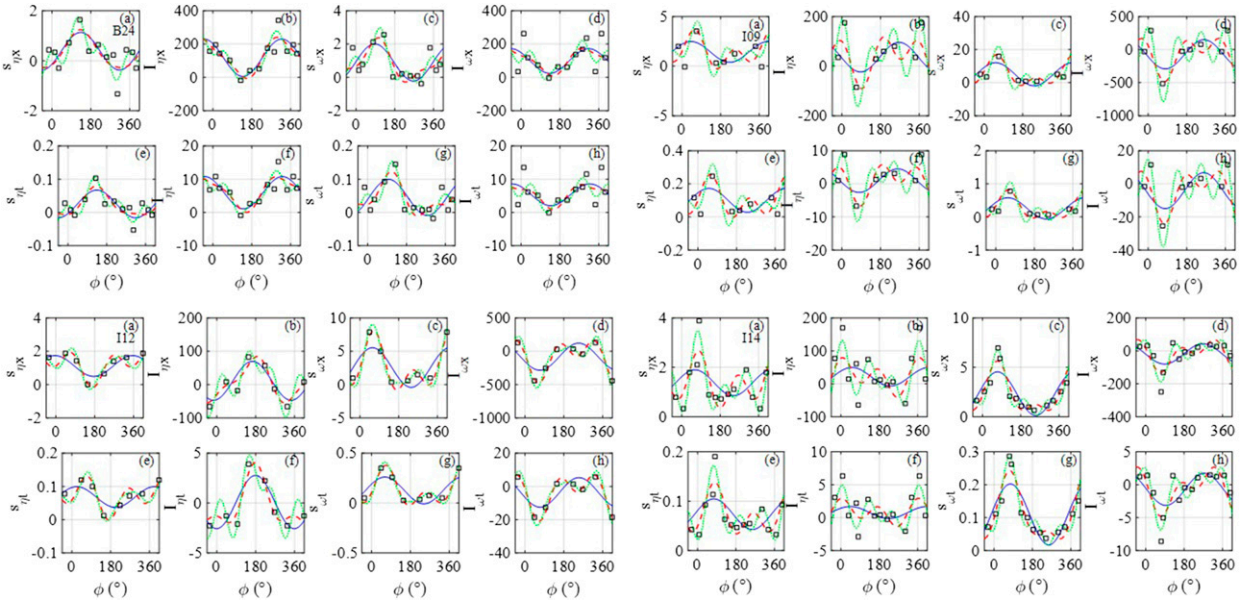

FIG. 3. Slope s_q and intercept I_q of $q = s_q(\phi)r + I_q(\phi)$, where q can be $x_{\eta x}$, $x_{\omega x}$, $t_{\eta t}$ or $t_{\omega t}$. The results obtained from datasets B24, I09, I12, and I14 (Table 1) are shown in the four quadrants; upper left (UL), upper right (UR), lower left (LL), and lower right (LR), respectively. The solid, dashed and dotted curves corresponding to the first-, second-, and third-order Fourier series are also superimposed in each panel. For each dataset, s and I are plotted (a),(b) for $x_{\eta x}$, (c),(d) for $x_{\omega x}$, (e),(f) for $t_{\eta t}$, and (g),(h) for $t_{\omega t}$.

(Hwang and Walsh 2016). A "processing transect" is defined as those data within a 30° azimuthal pie slice, that is, $\phi = 0° \pm 15°, 30° \pm 15°, \ldots$, that include at least five data points falling within the specified r range (50 to 160 km) in the pie slice. The representative azimuth angle of the processing transect is the mean of the azimuth angles of the included data.

The slopes and intercepts can be decomposed as the Fourier series

$$q = a_0 + 2\sum_{n=1}^{N}(a_{n,q}\cos n\phi + b_{n,q}\sin n\phi), \tag{8}$$

where q can be $s_{\eta x}$, $I_{\eta x}$, $s_{\omega x}$, $I_{\omega x}$, $s_{\eta t}$, $I_{\eta t}$, $s_{\omega t}$ or $I_{\omega t}$. The curves computed with $N = 1, 2$, and 3 are superimposed on the data with solid, dashed, and dotted lines, respectively, in Fig. 3.

The harmonic parameters $a_{n,q}$ and $b_{n,q}$ are computed from the trapezoid rule of integration (the following equation is applicable for $n = 0$ to N):

$$a_{n,q} = \frac{1}{2\pi}\int_0^{2\pi} q\cos n\phi\, d\phi, \quad b_{n,q} = \frac{1}{2\pi}\int_0^{2\pi} q\sin n\phi\, d\phi. \tag{9}$$

The results processed from the four datasets show a systematic, quasi-linear variation with the radius to maximum wind r_m (Fig. 4):

$$Y = p_{1Y}r_m + p_{2Y}, \tag{10}$$

where Y represents $a_{n,q}$ and $b_{n,q}$ in (8). The fitting coefficients p_{1Y} and p_{2Y} are listed in Table 3. Interestingly, Young (1988) also shows that r_m plays an important role for scaling the effective fetches of different hurricanes [his (5)] based on the analysis of a synthetic dataset composed of numerical simulations with different hurricane advancing speed, maximum wind speed, and radius of maximum wind. Further discussion on several different fetch models is given in section 4e.

Equations (6) to (10) complete the scaling model of the effective fetch and duration for hurricanes. For the situation of using the 2D wind field to obtain the wave parameters and the subsequently derived air–sea energy and momentum exchanges, the following describes the procedure to get the effective fetch or duration:

(i) rotate the coordinates of the wind field to be referenced to the hurricane heading;
(ii) find r_m and obtain $a_{n,q}$ and $b_{n,q}$ by (10) using the p_{1Y} and p_{2Y} values listed in Table 3;
(iii) obtain $s_{\eta x}$, $I_{\eta x}$, $s_{\omega x}$ and $I_{\omega x}$; or $s_{\eta t}$, $I_{\eta t}$, $s_{\omega t}$ and $I_{\omega t}$ by (8); and
(iv) calculate the fetches or durations of wave height and wave period for any location inside hurricane by (6) or (7), respectively.

TABLE 2. Slope s and intercept I of the linear fitting coefficients of fetch and duration as a function of r; the headers s_ex, I_ex, s_ox, I_ox, s_et, I_et, s_ot, and I_ot represent $s_{\eta x}$, $I_{\eta x}$, $s_{\omega x}$, $I_{\omega x}$, $s_{\eta t}$, $I_{\eta t}$, $s_{\omega t}$, and $I_{\omega t}$.

B24											
phi	1.26×10^{1}	3.07×10^{1}	7.89×10^{1}	1.29×10^{2}	1.71×10^{2}	2.14×10^{2}	2.53×10^{2}	2.85×10^{2}	3.04×10^{2}	3.45×10^{2}	
s_ex	3.45×10^{-1}	-3.04×10^{-1}	7.19×10^{-1}	1.64	3.73×10^{-1}	6.36×10^{-1}	1.43×10^{-1}	2.30×10^{-1}	−1.33	4.39×10^{-1}	
I_ex	1.96×10^{2}	1.42×10^{2}	1.02×10^{2}	-1.83×10^{1}	4.16×10^{1}	5.21×10^{1}	1.75×10^{2}	1.53×10^{2}	3.41×10^{2}	1.57×10^{2}	
s_ox	4.32×10^{-1}	7.84×10^{-1}	2.12	2.57	2.91×10^{-2}	2.10×10^{-1}	9.13×10^{-2}	9.19×10^{-2}	-3.90×10^{-1}	1.77	
I_ox	2.64×10^{2}	1.18×10^{2}	7.26×10^{1}	−4.63	6.26×10^{1}	6.14×10^{1}	1.36×10^{2}	1.69×10^{2}	2.36×10^{2}	3.43×10^{1}	
s_et	7.01×10^{-3}	-7.78×10^{-3}	3.86×10^{-2}	1.03×10^{-1}	2.58×10^{-2}	3.38×10^{-2}	1.03×10^{-2}	1.46×10^{-2}	-5.29×10^{-2}	2.74×10^{-2}	
I_et	1.08×10^{1}	7.26	6.03	-8.72×10^{-1}	2.65	3.23	8.38	7.07	1.53×10^{1}	6.81	
s_ot	7.73×10^{-3}	3.89×10^{-2}	9.29×10^{-2}	1.45×10^{-1}	8.15×10^{-3}	1.45×10^{-2}	7.77×10^{-3}	9.63×10^{-3}	-1.86×10^{-2}	7.56×10^{-2}	
I_ot	1.36×10^{1}	6.12	5.11	-9.84×10^{-2}	3.71	3.65	6.91	7.64	1.15×10^{1}	2.37	
I09											
phi	1.18×10^{1}	6.72×10^{1}	1.59×10^{2}	1.95×10^{2}	2.46×10^{2}	3.42×10^{2}					
s_ex	-5.34×10^{-2}	3.54	3.06×10^{-1}	3.95×10^{-1}	1.24	2.00					
I_ex	1.75×10^{2}	-8.51×10^{1}	2.89×10^{1}	5.99×10^{1}	8.01×10^{1}	3.56×10^{1}					
s_ox	3.52	1.60×10^{1}	1.31	8.42×10^{-1}	9.09×10^{-1}	5.10					
I_ox	2.88×10^{2}	-5.14×10^{2}	-2.53×10^{1}	−3.09	8.06×10^{1}	-3.21×10^{1}					
s_et	1.59×10^{-2}	2.46×10^{-1}	3.36×10^{-2}	3.96×10^{-2}	7.83×10^{-2}	1.16×10^{-1}					
I_et	8.83	−6.69	1.33	2.83	3.14	9.76×10^{-1}					
s_ot	1.73×10^{-1}	7.74×10^{-1}	9.34×10^{-2}	6.28×10^{-2}	6.33×10^{-2}	2.35×10^{-1}					
I_ot	1.15×10^{1}	-2.54×10^{1}	−2.06	-4.40×10^{-1}	3.27	−1.75					
I12											
phi	4.41×10^{1}	9.65×10^{1}	1.47×10^{2}	2.23×10^{2}	2.68×10^{2}	3.26×10^{2}					
s_ex	1.87	1.44	3.01×10^{-3}	6.61×10^{-1}	1.40	1.62					
I_ex	8.22	-1.81×10^{1}	8.21×10^{1}	5.70×10^{1}	-1.34×10^{1}	-6.54×10^{1}					
s_ox	7.87	5.00	3.67×10^{-1}	5.83×10^{-1}	1.48	9.99×10^{-1}					
I_ox	-4.45×10^{2}	-2.57×10^{2}	3.09×10^{1}	3.67×10^{1}	-3.94×10^{1}	1.32×10^{2}					
s_et	1.20×10^{-1}	1.00×10^{-1}	1.20×10^{-2}	4.30×10^{-2}	7.16×10^{-2}	7.78×10^{-2}					
I_et	−1.28	−2.10	3.91	2.23	-9.08×10^{-1}	−2.28					
s_ot	3.49×10^{-1}	2.57×10^{-1}	2.87×10^{-2}	3.87×10^{-2}	7.45×10^{-2}	5.08×10^{-2}					
I_ot	-1.85×10^{1}	-1.26×10^{1}	1.56	1.48	−1.89	5.67					
I14											
phi	7.82	3.61×10^{1}	7.25×10^{1}	8.20×10^{1}	1.27×10^{2}	1.58×10^{2}	1.84×10^{2}	2.18×10^{2}	2.44×10^{2}	3.03×10^{2}	3.32×10^{2}
s_ex	3.34×10^{-1}	1.80	2.10	3.88	8.86×10^{-1}	7.77×10^{-1}	7.25×10^{-1}	9.22×10^{-1}	1.12	1.90	7.90×10^{-1}
I_ex	1.70×10^{2}	1.39×10^{1}	6.09×10^{1}	-6.34×10^{1}	7.43×10^{1}	7.59	1.26×10^{1}	−3.45	6.23	-5.99×10^{1}	7.77×10^{1}
s_ox	2.57	3.44	6.97	5.92	2.07	1.84	1.09	9.93×10^{-1}	6.77×10^{-1}	1.13	1.63
I_ox	3.23×10^{1}	-2.84×10^{1}	-2.48×10^{2}	-1.30×10^{2}	4.84×10^{1}	-4.91×10^{1}	−6.85	-1.50×10^{1}	2.12×10^{1}	3.67×10^{1}	2.63×10^{1}
s_et	3.20×10^{-2}	9.27×10^{-2}	1.14×10^{-1}	1.90×10^{-1}	6.34×10^{-2}	5.21×10^{-2}	4.67×10^{-2}	5.18×10^{-2}	5.46×10^{-2}	8.38×10^{-2}	4.23×10^{-2}
I_et	6.31	3.23×10^{-1}	2.22	−2.88	2.74	2.38×10^{-1}	4.03×10^{-1}	-2.54×10^{-1}	4.54×10^{-1}	−2.08	3.06
s_ot	1.11×10^{-1}	1.51×10^{-1}	2.86×10^{-1}	2.61×10^{-1}	1.15×10^{-1}	1.00×10^{-1}	6.31×10^{-2}	5.49×10^{-2}	3.71×10^{-2}	5.55×10^{-2}	7.22×10^{-2}
I_ot	1.41	−1.20	−8.62	−5.06	1.39	−2.34	-4.67×10^{-1}	-7.45×10^{-1}	1.04	1.48	1.22

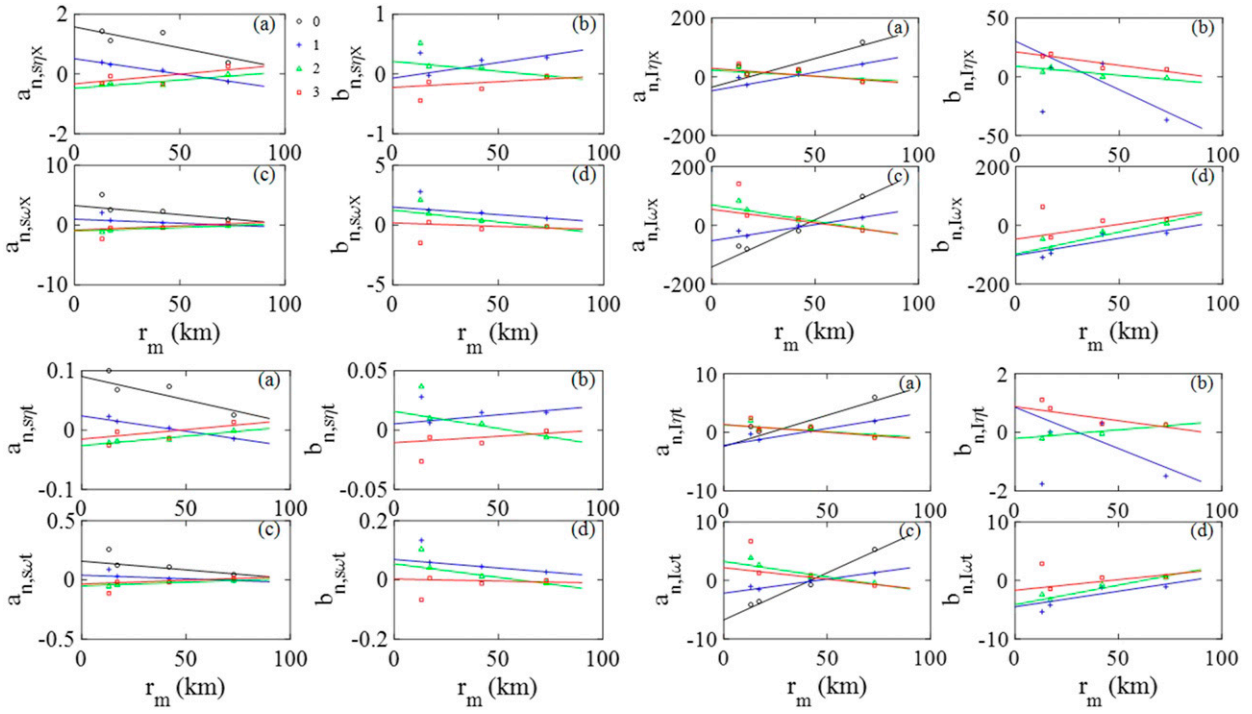

FIG. 4. Harmonic representations $q = \sum_{n=0}^{N}(a_{n,q}\cos n\phi + b_{n,q}\sin n\phi)$ of the slopes and intercepts of the linear functions defining the fetch and duration, where q can be $s_{\eta x}$, $I_{\eta x}$, $s_{\omega x}$, $I_{\omega x}$, $s_{\eta t}$, $I_{\eta t}$, $s_{\omega t}$ or $I_{\omega t}$. The harmonics $a_{n,q}$ and $b_{n,q}$ show linear dependence on r_m, $n = 0, 1, 2, 3$ ($b_{0,q} = 0$). (UL) Slopes of fetch for wave height and wave period: (a) $a_{n,s\eta x}$, (b) $b_{n,s\eta x}$, (c) $a_{n,s\omega x}$, and (d) $b_{n,s\omega x}$. (UR) Intercepts of fetch for wave height and wave period: (a) $a_{n,I\eta x}$, (b) $b_{n,I\eta x}$, (c) $a_{n,I\omega x}$, and (d) $b_{n,I\omega x}$. (LL) Slopes of duration for wave height and wave period: (a) $a_{n,s\eta t}$, (b) $b_{n,s\eta t}$, (c) $a_{n,s\omega t}$, and (d) $b_{n,s\omega t}$. (LR) Intercepts of duration for wave height and wave period: (a) $a_{n,I\eta t}$, (b) $b_{n,I\eta t}$, (c) $a_{n,I\omega t}$, and (d) $b_{n,I\omega t}$.

4. Discussion

a. *Wind-wave triplets, air–sea exchanges, and growth functions*

Given the fetch or duration information, the key information of H_s and T_p can be calculated from the growth functions with the U_{10} input (Hwang 2016; Hwang and Walsh 2016):

$$H_{sw} = 8.10\times10^{-4}U_{10}^{1.19}x_{\eta x}^{0.405},$$
$$T_{pw} = 9.28\times10^{-2}U_{10}^{0.526}x_{\omega x}^{0.237}, \quad \text{and} \qquad (11)$$
$$H_{sw} = 1.55\times10^{-4}U_{10}^{1.47}t_{\eta t}^{0.531},$$
$$T_{pw} = 3.53\times10^{-2}U_{10}^{0.690}t_{\omega t}^{0.310}. \qquad (12)$$

The subscript w is added to the wave variables in (11) and (12) to emphasize that the wave growth functions yield the wind-sea components of the surface waves. Figure 5 presents the scatterplots comparing the SRA-measured H_s and T_p and those calculated with the wave growth functions using the modeled fetch and duration. The four columns from left to right are wave height from fetch-limited growth function, wave height from duration-limited growth function, wave period from fetch-limited growth function, and wave period from duration-limited growth function (labeled H_{sf}, H_{sd}, T_{pf}, and T_{pd}, respectively, at the lower-right corner in the top row of Fig. 5). For reference, also shown in the figure are the dashed lines corresponding to 1:1 agreement, and the dotted lines are the 20% envelops, that is, [1.2:1 and 1:1/1.2].

The four rows from top to bottom are cases B24, I09, I12, and I14. Different plotting symbols are used for data in different quarters of the hurricane coverage area (green diamond, blue square, black circle, and red triangle for front, left, back, and right quarters, respectively; see Fig. 2, inset). The mean and standard deviation of the ratio between the modeled and the measured quantities are printed at the lower edge of each panel; these statistics are calculated with the data points with r between 45 and 200 km to exclude regions with severe contamination from nonlocal swells (Hwang 2016; Hwang and Walsh 2016).

The ranges of the mean and standard deviation of the ratios are very good for cases B24 and I14 (rows 1 and 4)—0.97 to 1.02 and 0.07 to 0.14, respectively—and good for cases I09 and I12 (row 2 and 3)—0.81 to 1.06 and 0.09

TABLE 3. Linear fitting coefficients of fetch and duration harmonics as a function of radius of maximum winds $Y = p_{1\gamma} r_m + p_{2\gamma}$ (8), where Y represents $a_{n,q}$ and $b_{n,q}$ in (7), and $n = 0, 1, 2, 3$ ($b_{0,q} = 0$); the headers s_ex, I_ex, s_ox, I_ox, s_et, I_et, s_ot, and I_ot represent $s_{\eta x}$, $I_{\eta x}$, $s_{\omega x}$, $I_{\omega x}$, $s_{\eta t}$, $I_{\eta t}$, $s_{\omega t}$, and $I_{\omega t}$.

q	s_ex	I_ex	s_ox	I_ox	s_et	I_et	s_ot	I_ot
a0,q								
p1	-1.40×10^{-2}	1.95	-3.04×10^{-2}	3.22	−7.88E-04	1.07×10^{-1}	-1.47×10^{-3}	1.60×10^{-1}
p2	1.57	-3.54×10^{1}	3.27	-1.42×10^{2}	9.04×10^{-2}	−2.42	1.58×10^{-1}	−6.73
a1,q								
p1	-1.02×10^{-2}	1.26	-1.34×10^{-2}	1.09	−5.17E-04	5.76×10^{-2}	−6.11E-04	4.81×10^{-2}
p2	5.10×10^{-1}	-4.77×10^{1}	9.85×10^{-1}	-5.22×10^{1}	2.39×10^{-2}	−2.23	3.99×10^{-2}	−2.18
b1,q								
p1	5.21×10^{-3}	-8.23×10^{-1}	-1.27×10^{-2}	1.16	1.54E-04	-2.81×10^{-2}	−5.75E-04	5.30×10^{-2}
p2	-6.87×10^{-2}	3.02×10^{1}	1.51	-1.02×10^{2}	5.25×10^{-3}	8.52×10^{-1}	6.90×10^{-2}	−4.50
a2,q								
p1	5.55×10^{-3}	-4.11×10^{-1}	1.23×10^{-2}	−1.10	3.22E-04	-2.31×10^{-2}	6.14E-04	-5.28×10^{-2}
p2	-4.79×10^{-1}	2.25×10^{1}	−1.01	6.93×10^{1}	-2.63×10^{-2}	1.27	-4.91×10^{-2}	3.24
b2,q								
p1	-3.32×10^{-3}	-1.52×10^{-1}	-2.00×10^{-2}	1.51	−2.88E-04	5.96×10^{-3}	−9.14E-04	6.68×10^{-2}
p2	2.11×10^{-1}	8.86	1.26	-9.80×10^{1}	1.58×10^{-2}	-2.16×10^{-1}	5.43×10^{-2}	−4.14
a3,q								
p1	6.44×10^{-3}	-5.32×10^{-1}	1.45×10^{-2}	-9.21×10^{-1}	3.19E-04	-2.61×10^{-2}	6.23E-04	-3.91×10^{-2}
p2	-3.29×10^{-1}	2.85×10^{1}	-8.47×10^{-1}	5.45×10^{1}	-1.52×10^{-2}	1.31	-3.41×10^{-2}	2.18
b3,q								
p1	1.91×10^{-3}	-2.28×10^{-1}	-5.70×10^{-3}	1.01	1.09E-04	-9.53×10^{-3}	−1.37E-04	3.62×10^{-2}
p2	-2.25×10^{-1}	2.11×10^{1}	1.80×10^{-1}	-4.71×10^{1}	-1.06×10^{-2}	8.72×10^{-1}	3.06×10^{-3}	−1.68

to 0.24, respectively. Several factors may have contributed to the performance difference in the model computations: (i) As shown in Fig. 1 and Table 2, B24 and I14 contain 10 to 11 processing transects inside the hurricane coverage region (compared to 6 for I09 and I12), thus providing a better azimuthal resolution for resolving the Fourier coefficients [(8), (9)] used for the fetch and duration models (Fig. 3). (ii) Between the two cases with six processing transects, results from I12 are better than those from I09, probably because of the more uniform distribution of the six processing transects in I12 compared to those irregular ones in I09 (Fig. 1). (iii) I09 tracks show many zigzag paths signifying aircraft maneuvering that may have caused data quality deterioration. (iv) The linear dependence on r_m for the Fourier components $a_{n,q}$ and $b_{n,q}$ (Fig. 4) may be overly simplified, but a more elaborate design would require more than four cases available for the present analysis. We hope that eventually more datasets of wind-wave triplets inside hurricanes will become available to refine the fetch and duration scaling model.

With wind-wave triplets (U_{10}, H_s, and T_p) available, the total energy and momentum exchange rates across the air–sea interface can be computed (Hwang and Sletten 2008; Hwang and Walsh 2016):

$$E_t = \alpha_E \rho_a U_{10}^3; \quad \alpha_E = 0.20 \omega_\#^{3.3} \eta_\#, \quad \text{and} \tag{13}$$

$$M_t = \alpha_M \rho_a U_{10}^2; \quad \alpha_M = 0.40 \omega_\#^{4.3} \eta_\#. \tag{14}$$

Figure 6 compares E_t and M_t calculated with the wind-wave triplets from hurricane hunter measurements and those with wave properties computed through the wave growth functions using the U_{10} input and modeled fetch and duration. The four columns from left to right are for E_t by the fetch functions, E_t by the duration functions, M_t by the fetch functions, and M_t by the duration functions. The four rows are B24, I09, I12, and I14 from top to bottom.

Similar to Fig. 5, the mean and standard deviation of the ratios between the modeled E_t and M_t and the references are printed at the lower edge of each panel. For cases B24 and I14 (rows 1 and 4), the ranges of the mean and standard deviation of the ratios are 1.02 to 1.15 and 0.16 to 0.45, respectively; for cases I09 and I12 (rows 2 and 3), they are 1.04 to 2.44 and 0.28 to 5.28, respectively. In general, the computed results using the fetch model contain more outliers and the statistics are worse than those using the duration model. The exact cause for this difference in performance using the fetch and duration functions is not clear at this stage. The duration computation is judged to be more accurate at the present state of modeling the effective fetch and duration.

b. *Temporal evolution of air–sea exchanges*

The two growth functions each for the fetch- and duration-limited conditions provide a means to obtain the full set of wind-wave triplets (U_{10}, H_s, and T_p) with only one of the three measured. At the present, time series of 2D hurricane wind fields are routinely

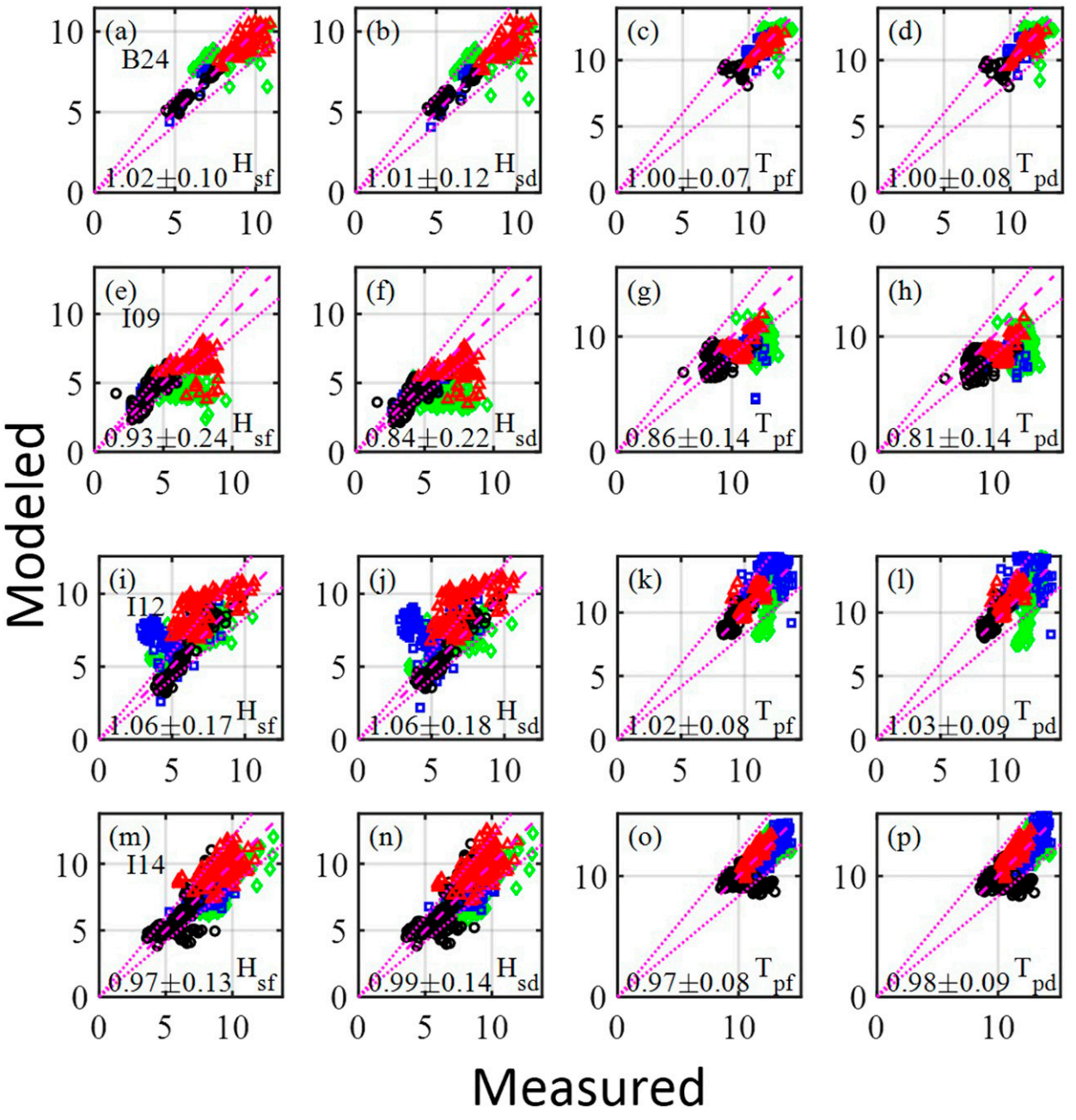

FIG. 5. Comparison of measurements and modeled wave height and wave period using the fetch- and duration-limited growth functions. (column 1) H_s using the fetch growth function, (column 2) H_s using the duration growth function, (column 3) T_p using the fetch growth function, and (column 4) T_p using the duration growth function. Cases B24, I09, I12, and I14 are arranged from top to bottom.

generated by the NOAA HRD real-time wind analysis (HWIND); the spatial resolution of these wind fields available in the legacy data archive site is nominally 6 km × 6 km. By taking advantage of the similarity relationship of the wind-wave triplets under fetch- and duration-limited growth, the key wave parameters (H_s and T_p) as well as the air–sea energy and momentum exchange rates (E_t and M_t) can be computed to evaluate the complex azimuthal and radial variations of these variables.

Here, we show the temporal evolution of the wave and air–sea interaction properties derived from the time series of Ivan 2004 wind fields. The time series covers the duration between 1930 UTC 6 September and 1500 UTC 16 September. A detailed modeling study of this hurricane has been reported by Fan et al. (2009); the

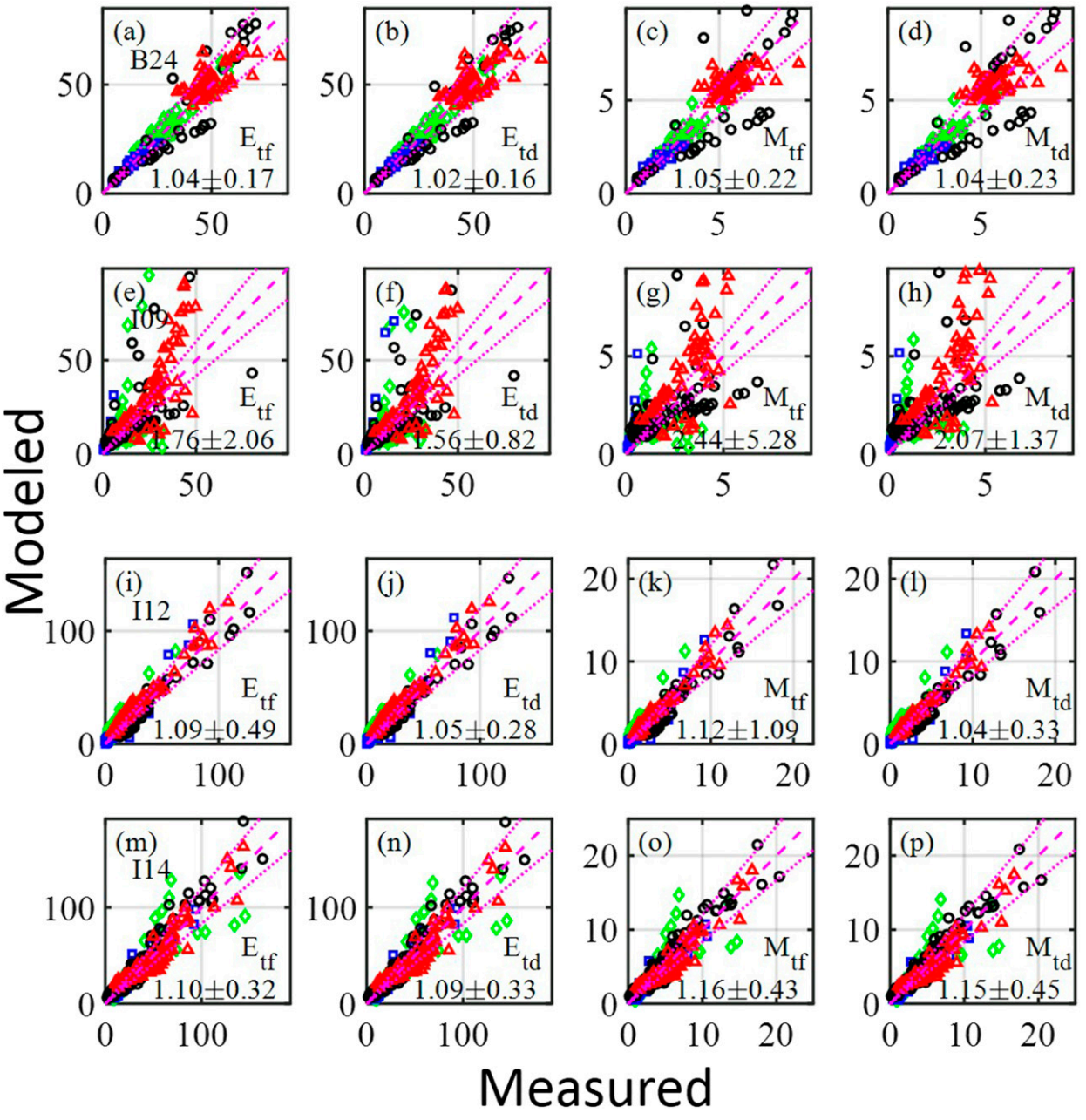

FIG. 6. As in Fig. 5, but for (column 1) E_t using the fetch growth function, (column 2) E_t using the duration growth function, (column 3) M_t using the fetch growth function, and (column 4) M_t using the duration growth function.

modeled waves compare very well with measurements from three hurricane hunter deployments (I09, I12, and I14 in Table 1). Figure 7 shows some basic information about the wind field time series, including the following:

1) (Fig. 7a) Maximum wind speed U_{10m}: The wind speeds corresponding to the thresholds of categories 1 to 5 of the Saffir–Simpson hurricane wind scale (33, 43, 50, 58, and 70 m s^{-1}) are shown with dashed lines. Over a long stretch of the record time, the hurricane is in categories 4 and 5.
2) (Fig. 7b) Radius of maximum wind r_m: The hurricane maintains a tight core with r_m less than 20 km most of the time prior to 13 September; the r_m then increases to about 40 km with some fluctuation.
3) (Fig. 7c) Azimuth angle of the position of maximum wind with respect to the hurricane heading ϕ_m: The position of the maximum wind is mostly on the right

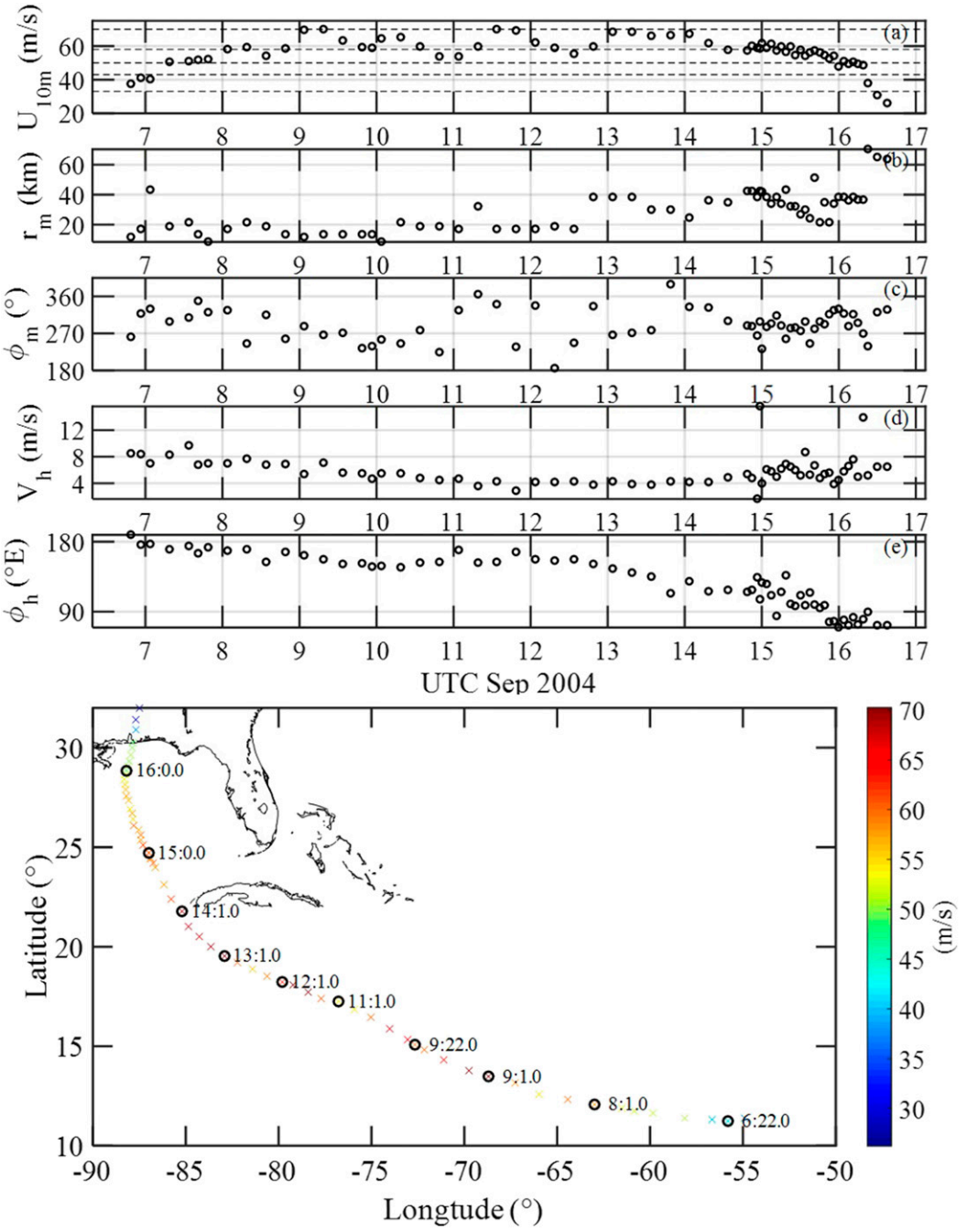

FIG. 7. Some basic information extracted from the time series of 2D wind fields for Hurricane Ivan 2004 discussed in this paper: (a) U_{10m}, (b) r_m, (c) ϕ_m, (d) V_h, and (e) ϕ_h. (bottom) The coordinates of the hurricane centers color coded with the maximal wind speed. The locations closest to daily 0000 UTC are circled and the time printed in the format (day):(decimal hour).

front quarter, but it also shifts slowly back and forth between the rear and front quarters on the right half plane in a somewhat random fashion; in two instances, the locations of maximum wind are in the left front quarter.

4) (Fig. 7d) Hurricane translation speed V_h: It starts out at about 8 m s^{-1}, decreases to about 4 m s^{-1}, then increases back to about 6 to 8 m s^{-1} over the period of the record.
5) (Fig. 7e) Direction of hurricane translation ϕ_h with respect to east (positive CCW): The hurricane

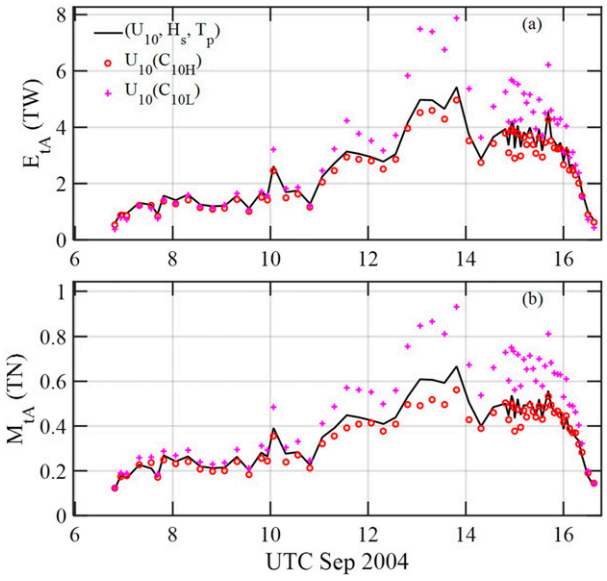

FIG. 8. Time series of (a) E_{tA} and (b) M_{tA} calculated with the energy and momentum balance equations combined with the duration-limited wave growth functions and comparison with computations using U_{10} alone combined with two different formulas of the bulk coefficients; see text for further detail.

moves steadily toward west then northwest and north.

6) [Fig. 7 (bottom)] A map of the hurricane trajectory: The hurricane center is identified with an x and the color of the marker corresponds to the maximum wind speed; the ones with times closest to daily 0000 UTC are circled, the time printed is in the format (day):(decimal hour).

The energy and momentum exchanges computed with the duration model and integrated over the hurricane coverage areas, E_{tA} and M_{tA}, respectively, are shown in Fig. 8 with black solid curves; the circular area of integration is centered at the hurricane eye with a 250-km radius.

To examine the impact of the wave factors, the energy and momentum exchanges are estimated with U_{10} alone. Two sets of computations are presented; the first set uses the mean energy exchange coefficient and the bulk drag coefficient formula described in Hwang and Walsh (2016):

$$E_{tUH} = \langle \alpha_E \rangle \rho_a U_{10}^3; \quad \langle \alpha_E \rangle = 4.7 \times 10^{-4}, \quad \text{and} \tag{15}$$

$$M_{tUH} = C_{10H} \rho_a U_{10}^2;$$

$$C_{10H} = 10^{-5}(-0.16U_{10}^2 + 9.67U_{10} + 80.58). \tag{16}$$

The second set uses the drag coefficient formula described in Liu et al. (2008) for the momentum exchange:

$$M_{tUL} = C_{10L} \rho_a U_{10}^2; \quad C_{10L} = 10^{-3}(0.069U_{10} + 0.73). \tag{17}$$

The energy exchange is computed by

$$E_{tUL} = 3.5 \rho_a u_*^3; \quad u_* = C_{10L}^{0.5} U_{10}. \tag{18}$$

The integrated energy and momentum exchange rates over the hurricane coverage area computed with wind speed input alone are shown in Fig. 8 with red circles for the first set and magenta pluses for the second set.

All three sets of exchange computations {I: energy and momentum exchanges considering U_{10}, H_s, and T_p [(13)–(14)]; II: U_{10} only with bulk coefficients [(15)–(16)]; and III: U_{10} only with bulk coefficients [(17)–(18)]} show a clear temporal evolution, with a generally increasing trend continuing to just before 14 September, at the time the strongest wind speed is 66.4 m s^{-1}. Interestingly, the energy and momentum exchanges are much weaker during the two earlier periods with much stronger maximum winds: 69.5 to 70.2 m s^{-1} at 0130 and 0730 UTC 9 September and 69.9 to 69.1 m s^{-1} at 1330 and 1930 UTC 11 September. This point will be further discussed in the next subsection when the spatial distributions are described.

Notably, during the earlier period before about 11 September, the three sets of computations produce very similar results, suggesting that the wave effects are relatively moderate during the earlier period. As time increases, the three computations diverge, and different choices of the drag coefficient and energy exchange coefficient can produce large differences in the computed exchanges.

c. *Ocean surface drag coefficient, spatial variation, and wave modification*

Our main purpose of investigating the effective fetch and duration for the hurricane wind field is to extract the surface wave information because many air–sea interaction processes are modified by the surface wave conditions. Here, we present an example of using the wind-wave growth functions to derive the spatial patterns of the wave parameters and the relevant air–sea exchange rates from the wind input.

Figure 9a shows the 2D wind field of Ivan 2004 at 1330 UTC 13 September. Using the information from the temporal analysis (section 4b), the wind field is rotated such that the heading is toward the top of the page. The maximum wind speed and its coordinates relative to the heading (marked with a red plus symbol in the figure) as well as the integrated exchanges over the 250-km circle are (U_{10m}, r_m, ϕ_m, E_{tA}, M_{tA}) = (66.3 m s^{-1}, 35 km, 278°, 4.95 TW, 0.66 TN). The energy and momentum

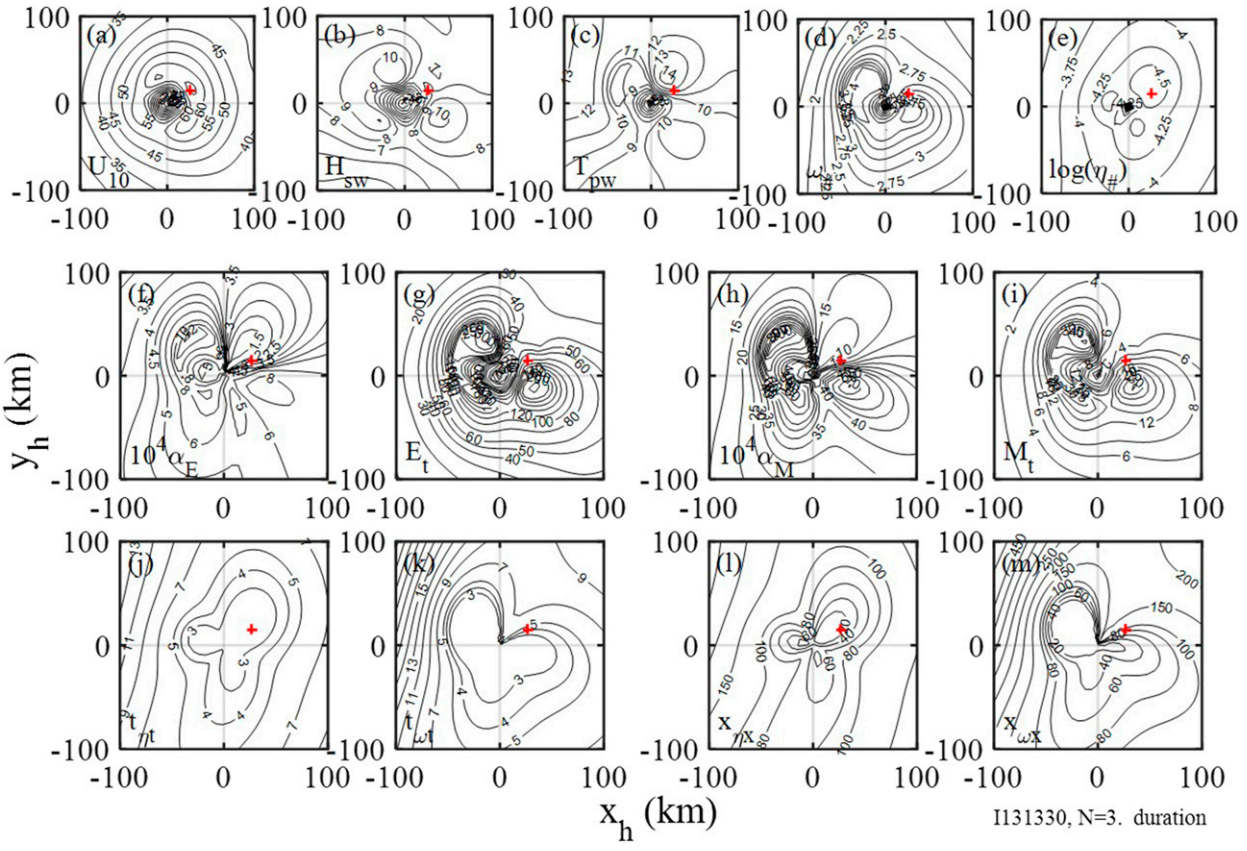

FIG. 9. Wave and air–sea exchange properties derived from the hurricane wind field: (a) the input HRD U_{10} field for Hurricane Ivan at 1330 UTC 13 Sep 2004; the output includes wave and air–sea exchange fields of (b) H_{sw}, (c) T_{pw}, (d) $\omega_{\#}$, (e) $\log(\eta_{\#})$, (f) α_E, (g) E_t, (h), α_M, and (i) M_t. The bottom row shows the durations and fetches: (j) $t_{\eta t}$, (k) $t_{\omega t}$, (l) $x_{\eta x}$, and (m) $x_{\omega x}$; all quantities are in MKS units except durations in (j) and (k) are given in h and fetches in (l) and (m) are given in km.

exchanges of this case are among the highest in the time series (Fig. 8).

The procedure of surface wave and air–sea exchange computation starts with the calculation of the effective fetch or duration (section 3), from which the wave height and wave period are derived through the wave growth functions using the wind field as input to complete the wind-wave triplets (U_{10}, H_s, and T_p). The bottom row of Fig. 9 shows the duration and fetch ($t_{\eta t}$, $t_{\omega t}$, $x_{\eta x}$, and $x_{\omega x}$), and the top row shows the wind-wave triplets (the results of H_{sw} and T_{pw} based on the duration growth functions are shown here) and the dimensionless frequency and variance ($\omega_{\#}$ and $\eta_{\#}$). The middle row shows the coefficients and rates of energy and momentum exchanges (α_E, E_t, α_M, and M_t). They all display complex spatial patterns difficult to be expressed as some simple functions of the wind speed alone. In particular, the spatial patterns of H_{sw} and T_{pw} deviate significantly from the U_{10} distribution; the resulting exchange patterns in terms of α_E and α_M or E_t and M_t are very similar to the $\omega_{\#}$ pattern, showing strong intensities in the forward left and backward right sectors of the hurricane for this wind field. In the remaining of this subsection, we focus on the subject of momentum exchange coefficient α_M, which is also the ocean surface drag coefficient C_{10}.

From the fluid dynamics point of consideration, the drag coefficient is a dimensionless factor given as the ratio of the surface stress τ normalized by the ''free-stream'' velocity U_{∞} outside the boundary layer (e.g., Schlichting 1968):

$$C_d = \frac{\tau}{\rho_a U_{\infty}^2} = \frac{u_*^2}{U_{\infty}^2}. \tag{19}$$

Given that the marine boundary layer is modified by the surface wave motion and that the dynamic effects of surface waves decay exponentially with distance away from the air–sea interface at a decay rate scaled by the wavelength, it is logical to set the reference wind speed at some elevation proportional to the surface wavelength. For example, the dynamic pressure from the

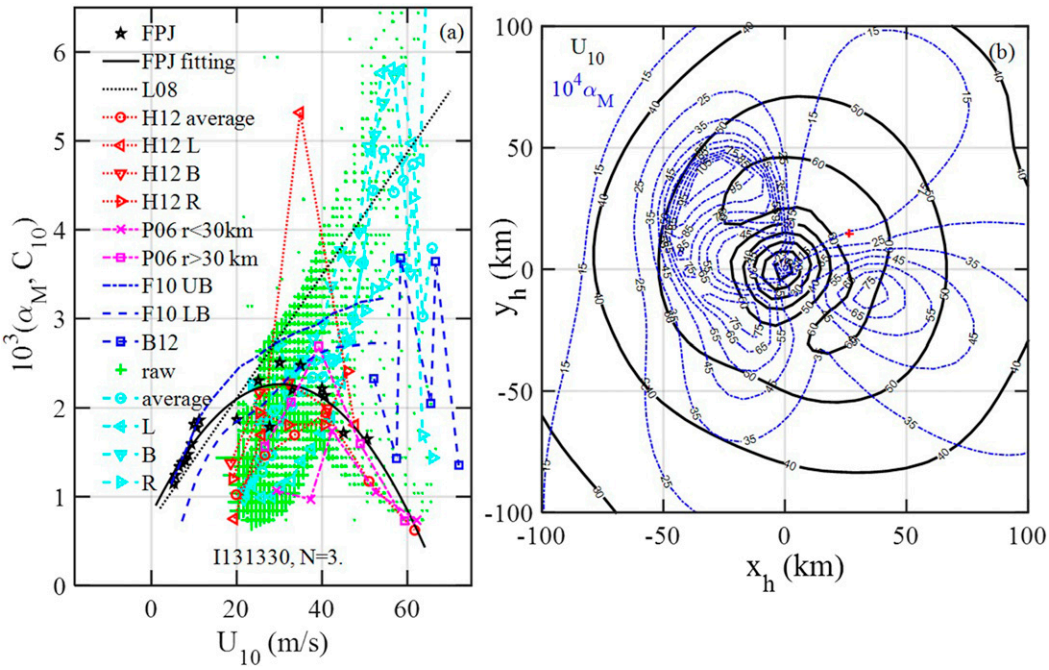

FIG. 10. (a) Comparison of the momentum exchange coefficient α_M (cyan symbols; raw data without azimuthal averaging are shown with green pluses in the background; the time of the hurricane wind field is at 1330 UTC 13 Sep 2004) with field observations of drag coefficient C_{10} emphasizing data collected in hurricane conditions (black, red, magenta and blue symbols); also shown in the figure are the C_{10} obtained from momentum flux computations (Fan et al. 2010; Bell et al. 2012). (b) Spatial distributions of U_{10} (black solid contours, labeled 10, 20, 30, ... m s^{-1}) and $10^4\alpha_M$ (blue dashed–dotted contours, labeled 5, 15, 25, ...).

wave motion is reduced to about 4% of the surface value at an elevation one-half of the surface wavelength, so $U_{\lambda/2}$ seems to be a suitable reference wind speed (e.g., Hwang 2004, 2006, and references therein).

To use the reference wind speed $U_{\lambda/2}$, the surface wave information is needed. Unfortunately, frequently the wind velocity is the only input of the environmental parameters for estimating the surface wind stress so the wind speed at a fixed elevation becomes the standard reference for normalizing the surface wind stress. For ocean applications, U_{10}, the neutral wind speed at 10-m elevation, has been used for reference; the corresponding surface drag coefficient is denoted as C_{10}. There are many empirical formulas expressing C_{10} as functions of U_{10}. Figure 10a shows a couple of them: the black solid and dotted lines are the empirical drag coefficient formulas given by (16) and (17), respectively. Also shown in the figure are field data collected in the open-ocean conditions with black (Felizardo and Melville 1995; Powell et al. 2003; Jarosz et al. 2007), red (Holthuijsen et al. 2012), and magenta (Powell 2006) symbols; except for those black data with $U_{10} < 15\,\mathrm{m\,s^{-1}}$, the measurements are collected inside hurricanes; more detailed discussions of these datasets have been given in Hwang and Walsh (2016).

The surface drag coefficient can be obtained from the momentum balance considerations. For example, Fan et al. (2010) show the wind speed dependency of the drag coefficient obtained from numerical computation of the air–sea momentum fluxes for hurricane wind conditions. The upper and lower bounds of their modeled results are shown with blue dashed–dotted and dashed curves respectively in Fig. 10a. Bell et al. (2012) calculate the C_{10} inside a hurricane using the conservation of azimuthally averaged absolute angular momentum in the atmospheric boundary layer. The results are shown with connected blue squares in Fig. 10a.

Hwang and Walsh (2016) consider the momentum balance of a wind-wave system, which yields parameterization equations of the momentum exchange rate and exchange coefficient given in (14). These parameterization functions allow the computation of the exchange and its coefficient at the same spatial resolution of the wind field, which is nominally 6 km × 6 km (Fig. 9). We have replotted the 2D maps of U_{10} and α_M in Fig. 10b, in which the contours of U_{10} and $10^4\alpha_M$ (or equivalently 10^4C_{10}) are shown in the same figure with solid black and dashed–dotted blue lines, respectively, the labeled contour values are (10, 20, ...) m s^{-1} for the former and (15, 25, ...) for the latter.

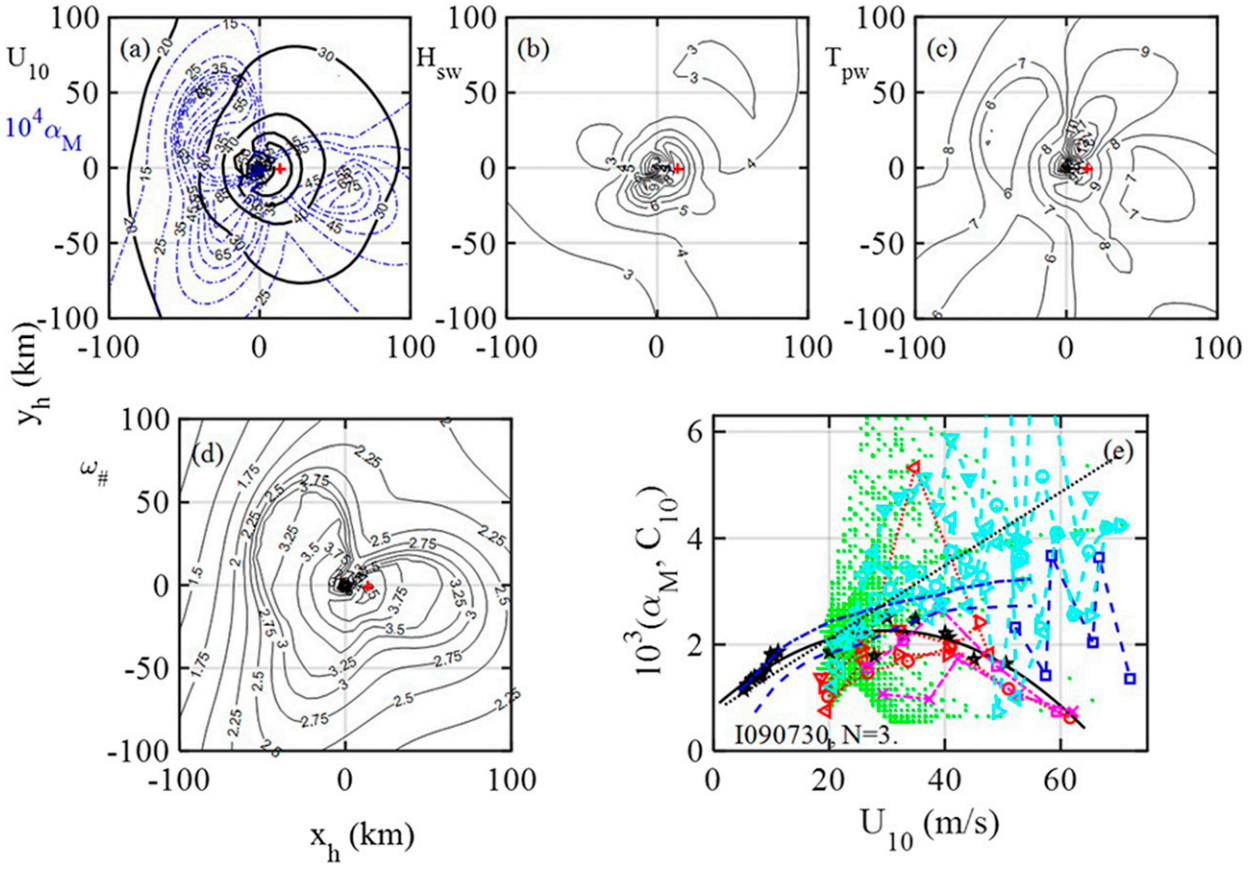

FIG. 11. (a) Spatial distributions of U_{10} (black solid contours, labeled 10, 20, 30, ... m s^{-1}) and $10^4\alpha_M$ (blue dashed–dotted contours, labeled 5, 15, 25, ...), (b) H_{sw}, (c) T_{pw}, (d) $\omega_{\#}$, and (e) comparison of the momentum exchange coefficient α_M (cyan symbols; green dots show raw data without azimuthal averaging) with field observations of drag coefficient C_{10} emphasizing data collected in hurricane conditions (black, red, magenta, and blue symbols). The time of the hurricane wind field (at 0730 UTC 09 Sep 2004) has the highest maximum wind speed (70.2 m s^{-1}) of the time series.

The complicated correlation between U_{10} and C_{10} is clearly illustrated in Fig. 10b. For example, the region with $U_{10} \geq 60\,\mathrm{m\,s^{-1}}$ forms a croissant-shaped enclosure that transects over areas of very low to very high C_{10} or α_M values. The maximum wind speed is in the right front quarter of the hurricane, and the location is marked with a red plus symbol in the contour map. As discussed earlier for Fig. 9, $(U_{10m}, r_m, \phi_m, E_{tA}, M_{tA}) = (66.3\,\mathrm{m\,s^{-1}}, 35\,\mathrm{km}, 278°, 4.95\,\mathrm{TW}, 0.66\,\mathrm{TN})$ for this case.

When the complex spatial distributions of U_{10} and C_{10} as illustrated in Fig. 10b is averaged over the whole region, the right, left, and back sectors, the results of $C_{10}(U_{10})$ of the various integrations are shown with cyan symbols in Fig. 10a. The largest data scatter among the different integrations as well as different datasets is in the very high wind speed region. To illustrate the point, the raw data without azimuthal averaging are displayed as green pluses in Fig. 10a with the marker size proportional to the data density within the (U_{10}, C_{10}) plotting grids; they scatter somewhat randomly with very wide spread in high winds. To reduce clutter and swell contamination, only data with $U_{10} > 20\,\mathrm{m\,s^{-1}}$ and $r < 250\,\mathrm{km}$ are displayed. It is interesting to observe that the apparent "outlier" C_{10} data spike reported in the Holthuijsen et al. (2012) hurricane analysis is in the left sector of the hurricane, consistent with the results shown in Fig. 10b.

The high wind speed range is also where most empirical formulations diverge, as demonstrated by the two empirical expressions superimposed in the figure: the black solid line for the second-order regression fitting [(16)] of the open-ocean observations by Felizardo and Melville (1995), Powell et al. (2003), and Jarosz et al. (2007) (FPJ) and the black dotted line for (17) by Liu et al. (2008). The wide spread C_{10} values for a narrow range of high wind speed band is in fact a feature very common in the hurricane wind field, as illustrated in the next two examples.

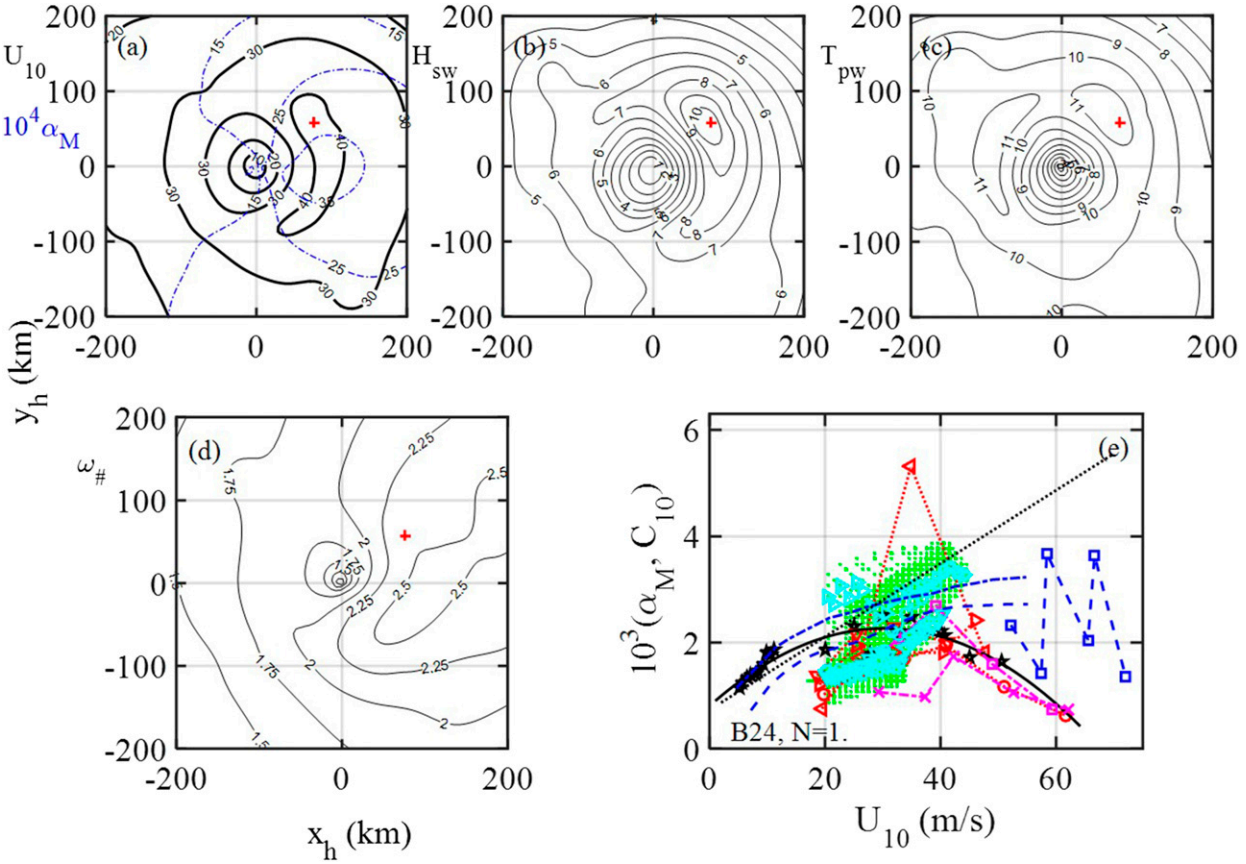

FIG. 12. As in Fig. 11, but for hurricane Bonnie at 1830 UTC 24 Aug 1998.

Figure 11 shows the results for Ivan 2004 at 0730 UTC 9 September. For simplicity, we present only the contour maps of the wind-wave triplets (Figs. 11a–c), the dimensionless frequency (Fig. 11d), and the momentum exchange coefficient, which is superimposed in the U_{10} field (Fig. 11a). This one has the largest maximum wind speed in the temporal sequence of the wind fields. It is at an earlier stage of development with a very small radius of maximum wind speed: $(U_{10m}, r_m, \phi_m, E_{tA}, M_{tA}) = (70.2\,\mathrm{m\,s^{-1}}, 13.5\,\mathrm{km}, 267°, 1.75\,\mathrm{TW}, 0.31\,\mathrm{TN})$. Although the maximum wind speed is the highest in the sequence, the integrated E_{tA} and M_{tA} are relatively small because of the tight and small region of high wind coverage. For example, the wind speed drops to about $30\,\mathrm{m\,s^{-1}}$ at $r \approx 100\,\mathrm{km}$, compared to about $40\,\mathrm{m\,s^{-1}}$ at the same distance for the case illustrated in Figs. 9 and 10 (1330 UTC 13 September). The corresponding wave height and wave period are also much weaker than those at 1330 UTC 13 September. Expressed as $C_{10}(U_{10})$, the average over the whole region, the right, left, and back sectors, are show in Fig. 11e with cyan symbols, and the raw data are shown with green dots; other datasets shown in the figure are the same as those in Fig. 10a. Very large variations are again observed in the high wind region, which reflects the complicated correlation between U_{10} and C_{10} as illustrated in Fig. 11a.

Figure 12 shows the results for Bonnie 1998 at 1830 UTC 24 August in the same format as Fig. 11. This wind field has a very large radius of maximum wind with the following basic information: $(U_{10m}, r_m, \phi_m, E_{tA}, M_{tA}) = (44.4\,\mathrm{m\,s^{-1}}, 95\,\mathrm{km}, 307°, 3.24\,\mathrm{TW}, 0.43\,\mathrm{TN})$. Although the maximum wind speed is relatively low at $44.4\,\mathrm{m\,s^{-1}}$, the E_{tA} and M_{tA} are comparable to those of Ivan 2004 around 11–12 September with maximum wind speed approaching $70\,\mathrm{m\,s^{-1}}$ (Figs. 7, 8). The average results of $C_{10}(U_{10})$ are show in Fig. 12e with cyan symbols, and the raw data are shown with green dots; the results again show that the complicated correlation between U_{10} and C_{10} as illustrated in Fig. 12a cannot be represented by some simply linear or nonlinear regression curves.

Although formulas of $C_{10}(U_{10})$ are likely to remain a constant presence in many air–sea interaction computations, such expressions are dimensionally inconsistent. Furthermore, the choice of 10 m as the reference elevation is mainly due to the necessity of standardization or convenience rather than the dynamic significance of that

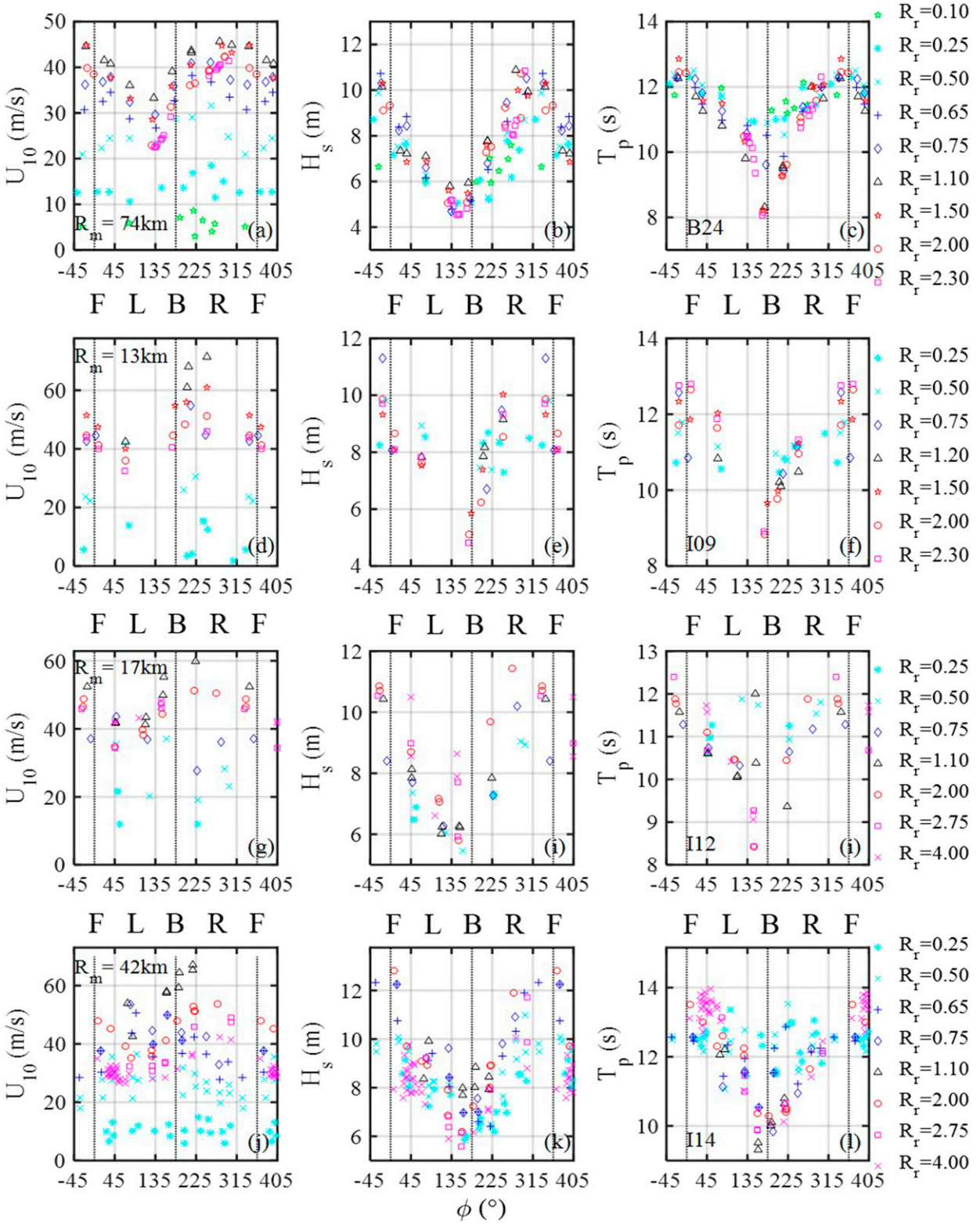

FIG. 13. Azimuthal variation of (left) U_{10}, (center) H_s, and (right) T_p at several radial distances shown as $R_r = r/r_m$ in the legend for cases B24, I09, I12, and I14 arranged from top to bottom.

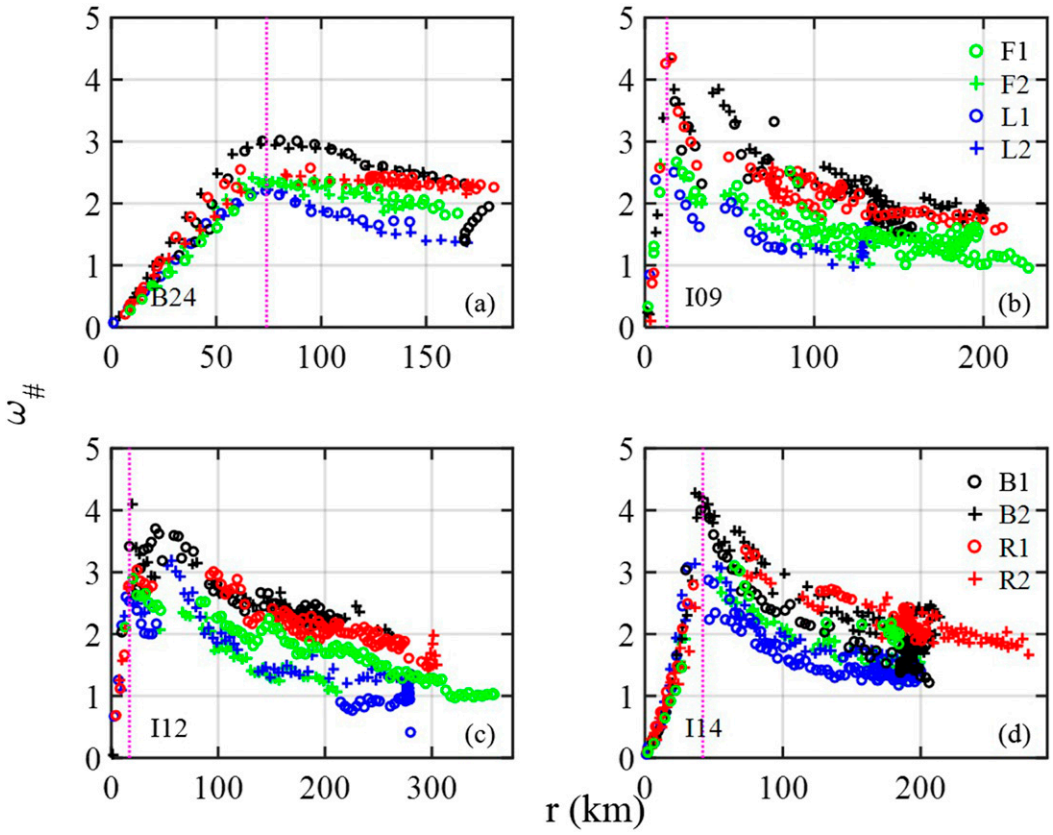

FIG. 14. Azimuthal and radial variation of the dimensionless frequency or inverse wave age inside hurricanes: (a) B24, (2) I09, (c) I12, and (d) I14. Data in eight different sectors (see Fig. 2 inset) are shown with different markers.

particular height in the marine boundary layer. From the fluid dynamics' considerations and dimensional analysis, we cannot expect a consistent similarity function to come out from such expressions. This is reflected on the very large number of $C_{10}(U_{10})$ formulas published in the literature; each one appears to show good agreement with a particular collection of measurements.

On the other hand, if the empirical $C_{10}(U_{10})$ formula is to be used for air–sea exchange computations, the analysis presented in Fig. 8 indicates that a nonmonotonic wind speed dependence with decreasing drag coefficient above approximately 35 m s^{-1} such as (16) indeed yields results closer to the calculations incorporating U_{10}, H_s, and T_p.

d. *Azimuthal and radial variations of hurricane wind and wave properties*

The simultaneous wind and wave data collected in several hurricane hunting missions provide us a rare opportunity to investigate the wave growth properties in the interior of hurricanes. The most significant result derived from our analyses is the conformation of the wave development following the same growth functions established for steady wind forcing conditions in the majority region of the hurricane interior.

Another important result derived from analyzing these simultaneous wind and wave data are the spatial distribution of the wind and waves properties. In particular, significant differences in the azimuthal distributions between wind speed, wave height, and wave period are noticed for the Hurricane Bonnie 1998 dataset (B24); the locations of the high and low are about (315°, 135°) for wind speed, shifting slightly CCW for wave height, and become close to (0°, 180°) for wave period (Hwang and Walsh 2016). The results are reproduced in Figs. 13a–c, showing the azimuthal distributions of U_{10}, H_s, and T_p at several radial distances normalized at $R_r = r/r_m$. We have done the same processing of azimuthal variation for the Ivan 2004 datasets I09, I12, and I14 (Figs. 13d–l). The CCW shifting of wave properties from the wind speed distribution is very similar to that observed in B24, although the azimuthal resolution of I09 and I12 is less than satisfactory due to the small number (six) of radial transects.

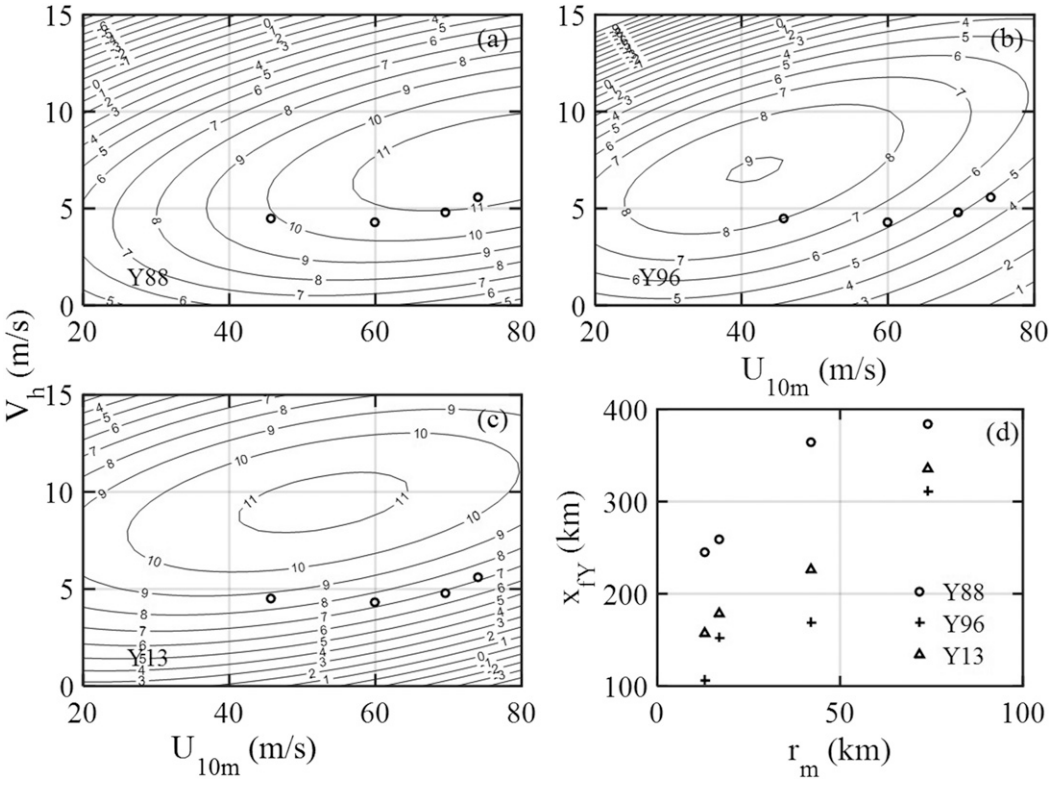

FIG. 15. The $f_2(U_{10m}, V_h)$ function of the effective fetch model of (a) Young (1988), (b) Young and Burchell (1996), and (c) Young and Vinoth (2013) and (d) the resulting effective fetch of the four hurricane scenes discussed in this paper (Table 1). The corresponding f_2 values are also shown as circles in (a) to (c).

In terms of the dimensionless frequency or the inverse wave age, which is among the most important parameters in evaluating the air–sea energy and momentum exchanges, the youngest waves in the back quarter and oldest waves in the left quarter as observed in B24 are also generally applicable to Ivan 2004 datasets I09, I12, and I14, as illustrated in Fig. 14 showing the results in eight sectors (inset of Fig. 2).

The asymmetric distribution of wave properties showing much higher wave height and longer wavelength in the front section of the hurricane has also been discussed by Wright et al. (2001), Black et al. (2007), and Holthuijsen et al. (2012). Some of the discussion further includes the multiple spectral components in different sectors of the hurricane; for example, see Figs. 5, 12–14 in Wright et al. (2001), Figs. 9–10 in Black et al. (2007), and Figs. 9 and A1 in Holthuijsen et al. (2012). King and Shemdin (1978) represent another earlier work addressing the asymmetry of hurricane waves based on airborne synthetic aperture radar (SAR) measurements in several hurricane passes. The quantity of data is much smaller than the other three works mentioned above, and their SAR processing only yields wavelength and wave direction information of the SAR images. The complicated nonlinear motion effect on the SAR imaging of ocean surface waves was not fully appreciated at the time, so the difference of the directional and wavelength information between SAR images and surface waves was not discussed.

e. Comparison with other fetch models for hurricane wave calculation

The practice of applying fetch-limited wave growth in hurricane wind forcing condition has a long history (e.g., Bretschneider 1959, 1972; Bretschneider and Tamaye 1976; King and Shemdin 1978; Shemdin 1980; Young 1988; Young and Burchell 1996; Bowyer and MacAfee 2005; MacAfee and Bowyer 2005; Young and Vinoth 2013).

The primary concern of these models is to obtain the largest wave height for a given hurricane for the purpose of providing the design wave criteria. There is less emphasis on exploring the spatial distribution (azimuthal and radial variations) inside the hurricane. For example, the ''trapped-fetch waves'' model described in Bowyer and MacAfee (2005) and MacAfee and Bowyer (2005) focuses on the numerical computation in the right half plane of the hurricane (in the Northern

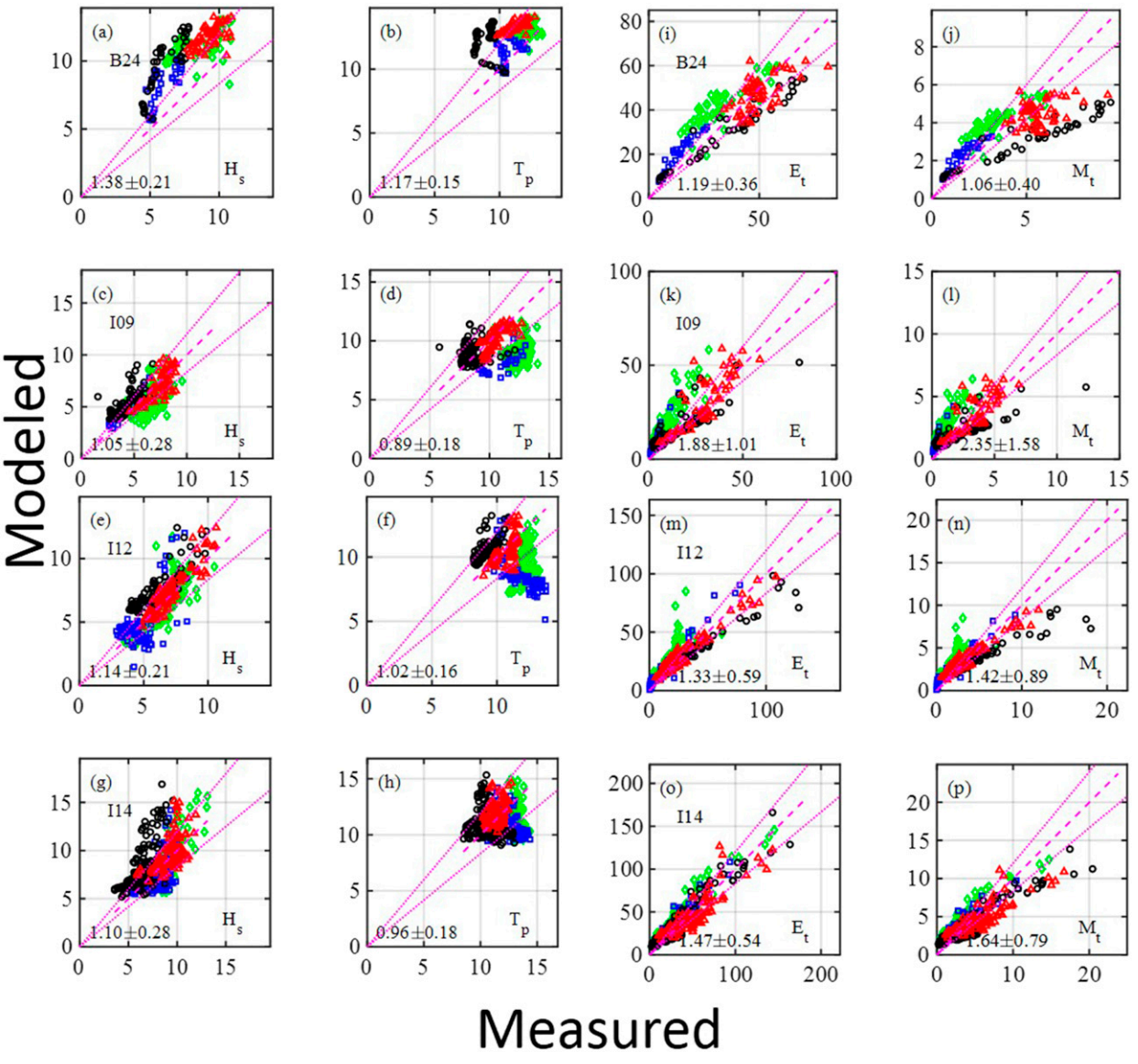

FIG. 16. Comparison of measurements and modeled H_s (first column), T_p (second column), E_t (third column) and M_t (fourth column) using the Young and Vinoth (2013) fetch model for B24, I09, I12, and I14, from top to bottom; they can be compared with the first and third columns of Figs. 5 and 6, which are computed with the fetch scaling model presented in section 3.

Hemisphere) because the forward motion enhances wind speed in that sector. Using a model wind field, the computation tracks wave development using the Bretschneider fetch growth functions for wave height and wave period as time increases and the wind field moves along. The wave is followed until it either outruns or falls behind the wind field. For the right condition when the wave group velocity matches the hurricane forward motion, the effective fetch can reach the 1000-km range with very high and long waves produced by relatively low winds; they have shown several examples of waves in excess of 20 m produced by winds of about 44 m s^{-1} (category 2 hurricane). The computation is in good agreement with nearby buoy recording. Unfortunately, because the V_h range in the available datasets is very limited (Table 1), we are unable to investigate its impact on our fetch and duration model described in section 3.

The hurricane fetch model developed by Young and colleagues (Young 1988; Young and Burchell 1996; Young and Vinoth 2013) can be applied to the instantaneous wind field without Lagrangian tracking of the wave development; therefore, they are more suitable for comparing with the fetch model described in

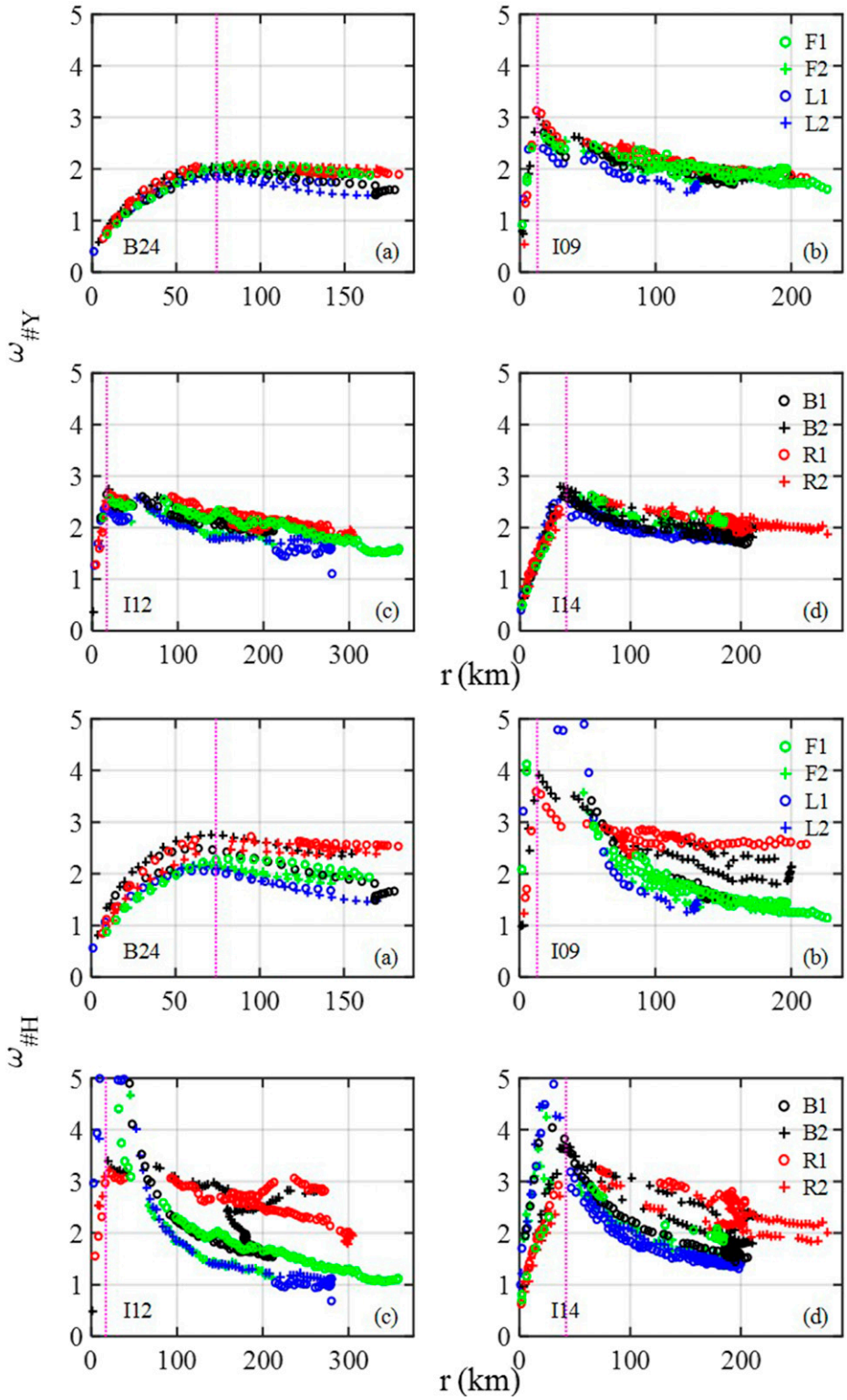

FIG. 17. As in Fig. 14, but the top four panels are computed with the Y13 fetch model and the bottom four panels are computed with the H fetch model (section 3).

this paper (section 3). Their fetch model can be expressed as

$$x_{fY} = f_1(r_m) f_2(U_{10m}, V_h), \tag{20}$$

where f_1 is a logarithmic function, and f_2 is a second-order bivariable polynomial function. The three versions of their fetch model, denoted as Y88, Y96, and Y13, subsequently, differ only in the coefficients of the f_2 polynomial function. Figures 15a, 15b, and 15c show respectively the three versions (Y88, Y96, and Y13) of the f_2 function. Figure 15d displays the resulting effective fetch for the four cases discussed in this paper (Table 1).

Applying Young's model fetch to the hurricane hunter wind measurements, the wave height, wave period, energy, and momentum exchange rates can be calculated as described earlier. Figure 16 shows H_s, T_p, E_t, and M_t computed with the Y13 fetch for the four datasets discussed in this paper. To compare with the computations using the fetch model described in section 3 (referred to as the H fetch model hereinafter), the left two columns correspond to the first and third columns of Fig. 5, and the right two columns correspond to the first and third columns of Fig. 6. As in Figs. 5 and 6, the mean and standard deviation of the ratio between the modeled and the measured quantities are printed at the lower edge of each panel.

Figure 17 shows the dimensionless frequency or the inverse wave age parameter calculated for the four hurricane hunter datasets; the top four panels are the results using the Y13 fetch model, and the bottom four panels are those using the H fetch model. The reference results obtained from the simultaneous wind and wave measurements are given in Fig. 14. Overall, the H fetch model produces more realistic spatial distribution of the wave parameters from the wind speed input.

5. Summary

Surface waves inside hurricanes are found to adhere to the fetch- and duration-limited nature of wind-wave growth. This opens up a door to a large wealth of knowledge derived from decades of wind-wave research. At the foundation of this wealth of knowledge is a pair of equations connecting the three critical wind and wave parameters: the wind-wave triplets (U_{10}, H_s, and T_p). The situation of ''two equations, three unknowns'' makes it feasible to obtain the full set of wind-wave triplets knowing only one of the three. Furthermore, the equations governing the energy and momentum balances of the wind-wave systems are given as functions of the wind-wave triplets; thus, the growth functions can be used to quantify the critical information of air–sea energy and momentum exchanges across the air–sea interface.

To access this vast wealth of knowledge, it is necessary to establish the effective fetch and duration of the hurricane wind field. Through reverse engineering using four sets of wind-wave triplets acquired in hurricane hunter missions, a scaling model for the effective fetch and duration is formulated. Computed wind-wave triplets using the growth functions coupled with the modeled fetch and duration are in good agreement with the wind-wave triplets obtained in hurricane hunter missions.

Applying the fetch and duration model to the time series of 2D hurricane wind fields, the temporal variation and spatial distribution of the wave properties and air–sea exchanges following the hurricane development can be studied in great detail.

Acknowledgments. This work is sponsored by the Office of Naval Research (Funding Doc. N0001416WX00044). We are grateful for the careful preservation of the SRA datasets and supporting information provided by Ed Walsh, and the service of HRD wind archive maintained in the HWIND legacy data site: pre-2014 data are available online (at http://www.rms.com/perils/hwind/legacy-archive/); for years 2014 and after, RMS has developed a research partnership policy for sharing commercial data with academic researchers. Academic researchers interested in accessing enhanced archive data, please send an email to support@rms.com. Datasets used in this analysis are given in the references cited. The processing codes and data segments can also be obtained by contacting the corresponding author.

REFERENCES

Babanin, A. V., and Y. P. Soloviev, 1998: Field investigation of transformation of the wind wave frequency spectrum with fetch and the stage of development. *J. Phys. Oceanogr.*, **28**, 563–576, doi:10.1175/1520-0485(1998)028<0563:FIOTOT>2.0.CO;2.

Bell, M. M., M. T. Montgomery, and K. A. Emanuel, 2012: Air–sea enthalpy and momentum exchange at major hurricane wind speeds observed during CBLAST. *J. Atmos. Sci.*, **69**, 3197–3222, doi:10.1175/JAS-D-11-0276.1.

Black, P. G., and Coauthors, 2007: Air–sea exchange in hurricanes: Synthesis of observations from the Coupled Boundary Layer Air–Sea Transfer experiment. *Bull. Amer. Meteor. Soc.*, **88**, 357–374, doi:10.1175/BAMS-88-3-357.

Bowyer, P. J., and A. W. MacAfee, 2005: The theory of trapped-fetch waves with tropical cyclones—An operational perspective. *Wea. Forecasting*, **20**, 229–244, doi:10.1175/WAF849.1.

Bretschneider, C. L., 1959: Hurricane design wave practices. *Trans. Amer. Soc. Civ. Eng.*, **124**, 39–62.

——, 1972: Revision to hurricane design wave practices. *Proc. 13th Coastal Eng. Conf.*, Vancouver, Canada, ASCE, 167–195.

——, and E. E. Tamaye, 1976: Hurricane wind and wave forecasting techniques. *Proc. 15th Coastal Eng. Conf.*, Honolulu, HI, ASCE, 202–237.

Burling, R. W., 1959: The spectrum of waves at short fetches. *Dtsch. Hydrogr. Z.*, **12**, 96–117, doi:10.1007/BF02019818.

Dobson, F., W. Perrie, and B. Toulany, 1989: On the deep-water fetch laws for wind-generated surface gravity waves. *Atmos.–Ocean*, **27**, 210–236, doi:10.1080/07055900.1989.9649334.

Donelan, M. A., J. Hamilton, and W. H. Hui, 1985: Directional spectra of wind-generated waves. *Philos. Trans. Roy. Soc. London*, **A315**, 509–562, doi:10.1098/rsta.1985.0054.

Fan, Y., I. Ginis, T. Hara, C. W. Wright, and E. J. Walsh, 2009: Numerical simulations and observations of surface wave fields under an extreme tropical cyclone. *J. Phys. Oceanogr.*, **39**, 2097–2116, doi:10.1175/2009JPO4224.1.

——, ——, ——, ——, and ——, 2010: Momentum flux budget across the air–sea interface under uniform and tropical cyclone winds. *J. Phys. Oceanogr.*, **40**, 2221–2242, doi:10.1175/2010JPO4299.1.

Felizardo, F., and W. K. Melville, 1995: Correlations between ambient noise and the ocean surface wave field. *J. Phys. Oceanogr.*, **25**, 513–532, doi:10.1175/1520-0485(1995)025<0513:CBANAT>2.0.CO;2.

Hasselmann, K., and Coauthors, 1973: Measurements of wind-wave growth and swell decay during the Joint North Sea Wave Project (JONSWAP). Ergänzungsheft zur Deutschen Hydrographischen Zeitschrift Reihe A(8) 12, 95 pp.

Holthuijsen, L. H., M. D. Powell, and J. D. Pietrzak, 2012: Wind and waves in extreme hurricanes. *J. Geophys. Res.*, **117**, C09003, doi:10.1029/2012JC007983.

Hwang, P. A., 2004: Influence of wavelength on the parameterization of drag coefficient and surface roughness. *J. Oceanogr.*, **60**, 835–841, doi:10.1007/s10872-005-5776-3.

——, 2006: Duration- and fetch-limited growth functions of wind-generated waves parameterized with three different scaling wind velocities. *J. Geophys. Res.*, **111**, C02005, doi:10.1029/2005JC003180.

——, 2016: Fetch- and duration-limited nature of surface wave growth inside tropical cyclones: With applications to air-sea exchange and remote sensing. *J. Phys. Oceanogr.*, **46**, 41–56, doi:10.1175/JPO-D-15-0173.1.

——, and D. W. Wang, 2004: Field measurements of duration-limited growth of wind-generated ocean surface waves at young stage of development. *J. Phys. Oceanogr.*, **34**, 2316–2326, doi:10.1175/1520-0485(2004)034<2316:FMODGO>2.0.CO;2; Corrigendum, **35**, 268–270, doi:10.1175/JPO-2731.1.

——, and M. A. Sletten, 2008: Energy dissipation of wind-generated waves and whitecap coverage. *J. Geophys. Res.*, **113**, C02012, doi:10.1029/2007JC004277; Corrigendum, **114**, C02015, doi:10.1029/2008JC005244.

——, and E. J. Walsh, 2016: Azimuthal and radial variation of wind-generated surface waves inside tropical cyclones. *J. Phys. Oceanogr.*, **46**, 2605–2621, doi:10.1175/JPO-D-16-0051.1.

Jarosz, E., D. A. Mitchell, D. W. Wang, and W. J. Teague, 2007: Bottom-up determination of air–sea momentum exchange under a major tropical cyclone. *Science*, **315**, 1707–1709, doi:10.1126/science.1136466.

King, D. B., and O. H. Shemdin, 1978: Radar observations of hurricane wave directions. *Proc. 16th Coastal Eng. Conf.*, Hamburg, Germany, ASCE, 209–226.

Liu, L. L., W. Wang, and R. X. Huang, 2008: The mechanical energy input to the ocean induced by tropical cyclones. *J. Phys. Oceanogr.*, **38**, 1253–1266, doi:10.1175/2007JPO3786.1.

MacAfee, A. W., and P. J. Bowyer, 2005: The modeling of trapped-fetch waves with tropical cyclones—A desktop operational model. *Wea. Forecasting*, **20**, 245–263, doi:10.1175/WAF850.1.

Moon, I.-J., I. Ginis, T. Hara, H. L. Tolman, C. W. Wright, and E. J. Walsh, 2003: Numerical simulation of sea surface directional wave spectra under hurricane wind forcing. *J. Phys. Oceanogr.*, **33**, 1680–1706, doi:10.1175/2410.1.

Powell, M. D., 2006: Drag coefficient distribution and wind speed dependence in tropical cyclones. NOAA JHT Program Final Rep., 26 pp.

——, S. H. Houston, and T. A. Reinhold, 1996: Hurricane Andrew's landfall in south Florida. Part I: Standardizing measurements for documentation of surface wind fields. *Wea. Forecasting*, **11**, 304–328, doi:10.1175/1520-0434(1996)011<0304:HALISF>2.0.CO;2.

——, P. J. Vickery, and T. A. Reinhold, 2003: Reduced drag coefficient for high wind speeds in tropical cyclones. *Nature*, **422**, 279–283, doi:10.1038/nature01481.

Schlichting, H., 1968: *Boundary-Layer Theory*. McGraw Hill, 748 pp.

Shemdin, O. H., 1980: Prediction of dominant wave properties ahead of hurricanes. *Proc. 17th Coastal Eng. Conf.*, Sydney, Australia, ASCE, 600–609.

Walsh, E. J., D. W. Hancock, D. E. Hines, R. N. Swift, and J. F. Scott, 1985: Directional wave spectra measured with the surface contour radar. *J. Phys. Oceanogr.*, **15**, 566–592, doi:10.1175/1520-0485(1985)015<0566:DWSMWT>2.0.CO;2.

——, ——, ——, ——, and ——, 1989: An observation of the directional wave spectrum evolution from shoreline to fully developed. *J. Phys. Oceanogr.*, **19**, 670–690, doi:10.1175/1520-0485(1989)019<0670:AOOTDW>2.0.CO;2.

Wright, C. W., and Coauthors, 2001: Hurricane directional wave spectrum spatial variation in the open ocean. *J. Phys. Oceanogr.*, **31**, 2472–2488, doi:10.1175/1520-0485(2001)031<2472:HDWSSV>2.0.CO;2.

Young, I. R., 1988: Parametric hurricane wave prediction model. *J. Waterw. Port Coastal Ocean Eng.*, **114**, 637–652, doi:10.1061/(ASCE)0733-950X(1988)114:5(637).

——, 1998: Observations of the spectra of hurricane generated waves. *Ocean Eng.*, **25**, 261–276, doi:10.1016/S0029-8018(97)00011-5.

——, 2003: A review of the sea state generated by hurricanes. *Mar. Struct.*, **16**, 201–218, doi:10.1016/S0951-8339(02)00054-0.

——, 2006: Directional spectra of hurricane wind waves. *J. Geophys. Res.*, **111**, C08020, doi:10.1029/2006JC003540.

——, and G. P. Burchell, 1996: Hurricane generated waves as observed by satellite. *Ocean Eng.*, **23**, 761–776, doi:10.1016/0029-8018(96)00001-7.

——, and J. Vinoth, 2013: An ''extended fetch'' model for the spatial distribution of tropical cyclone wind–waves as observed by altimeter. *Ocean Eng.*, **70**, 14–24, doi:10.1016/j.oceaneng.2013.05.015.